Toward Ultrafast Spin Dynamics in Low-Dimensional Semiconductors

DISSERTATION

Presented in Partial Fulfillment of the Requirements for the Degree Doctor of Philosophy in the Graduate School of The Ohio State University

By

Yi-Hsin Chiu

Graduate Program in Physics

The Ohio State University

2015

Dissertation Committee:

Professor Ezekiel Johnston-Halperin, Advisor

Professor Fengyuan Yang

Professor William Putikka

Professor Richard R. Freeman

Abstract

Since the discovery of long spin relaxation times of itinerant electrons up to 100 nanoseconds and spin diffusion lengths over 100 μm in GaAs, extraordinary advances in semiconductor spintronics have been made in the past one and half decades. Incorporating spins in semiconductors requires the following essential capabilities: (i) injection of spins into semiconductors, (ii) manipulation of spins, and (iii) sensitive detection of spin coherence.

The solutions to these challenges lie in a deeper understanding of spin interactions and spin relaxation in semiconductors as well as appropriate tools to probe spin dynamics. In particular, recent experiments have suggested the important role of dimensionality in spin dynamics. For example, spin-orbit interaction, the dominant source of spin relaxation in most II-VI and III-V semiconductors, has been shown to be significantly suppressed in reduced dimensions. Low-dimensional semiconductors are therefore appealing candidates for exploring spin physics and device applications.

This dissertation aims at exploring spin dynamics in low dimensional semiconductor systems using time-resolved optical techniques. The time resolution allows for a direct measurement of the equilibrium and non-equilibrium carrier spins and various spin interactions in the time domain. Optical approaches are also a natural fit for probing optically active nanostructures where electric approaches can often encounter challenges.

For instance, fabricating electric contacts with nanostructures is a proven challenge because of their reduced size and modified electronic structure.

This dissertation is divided into three sections targeting an ultimate goal of employing optical methods to explore spin dynamics in low dimensional semiconductors. First, the time-resolved Kerr rotation technique is employed to study spin relaxation in Fe/MgO/GaAs heterostructures. The results reveal rich interactions between the GaAs electron spins, nuclear spins, and the neighboring Fe spins, as well as the resulting exchange-driven electron spin relaxation in GaAs. This lays the groundwork for this dissertation to explore low dimensional systems.

Second, we work to facilitate optical studies of spin dynamics in one dimension (1D), which hasn't been possible in the past due to the fundamental challenge of optical polarization anisotropy. We propose a dielectric-matched membrane structure based on GaAs/AlGaAs core-shell nanowires. By simultaneous addressing the optical polarization anisotropy and various technical challenges, this study offers a promising route to optical investigations of 1D spin physics.

Third, a novel 2D material, germanane (GeH), is investigated by continuous wave (cw) polarization-resolved photoluminescence (PL) spectroscopy as a first step toward future ultrafast pump-probe study. PL develops a finite degree of circular polarization under circular excitation (optical orientation) or in an applied magnetic field (Zeeman effect), indicating the presence of spin-polarized carriers. This study presents the first magneto-optical investigation in germanane.

Dedication

This document is dedicated to my family.

Acknowledgments

The journey toward a Ph.D. is long, full of challenges and inspirations. When I sit down and look back, I couldn't be more grateful and surprised for so many brilliant minds I've encountered and so much generous help I've been given.

My deepest gratitude goes to my advisor Professor Ezekiel Johnston-Halperin. His guidance has benefited me greatly in my growth as a scientist. In particular, I appreciate his patience to allow me the space to make (sometimes silly) mistakes and grow. His full support has granted me the privilege to focus on my research without having to worry much about distractions. His passion for science is a great source of inspiration that have carried me throughout my graduate years and into my future career.

I would also like to thank my collaborators, Nicholas Minutillo, Greg Smith, Professor Fengyuan Yang, Shishi Jaing, Elisabeth Bianco, Professor Josh Goldberger, Patrick Odenthal, and Professor Roland Kawakami. I've had the opportunity to work with each of them closely and it has been a real pleasure. I thank them for sharing their valuable insights and making our collaborations fruitful.

My gratitude also goes to the many talented colleagues who have offered generous help with my Ph.D. research. From my group, Lei Fang, Howard Yu, Yu-Sheng Ou, Justin Young, Kurtis Wickey, Megan Harberts, Matt Sheffield, Mike Chilcote, Shawna Hollen,

Yong Pu, and Dongkyun Ko. Within the department, Jay Jung, Beth Bushong, Kelly Luo, Richelle Teeling-Smith, Vidya Bhallamudi, Rohan Adur, and Chris Wolfe.

Furthermore, I would like to acknowledge the support staff of the physics department, John Gosser, Josh Gueth, and Michael Graham from the machine shop, Richard Kent Ludwig from the low temperature shop, Denis Pelekhov and Camelia Selcu from the Center of Emergent Materials, Robert Merritt, Kris Dunlap, Amanda Zuurdeeg, and Jaimie Mollison. Without their outstanding expertise, my graduate career would be a lot more difficult.

I am also extremely lucky to have the company of many wonderful friends, Kimmy Young, Ssu-Yen Huang, Sheng Jiang, Hsiang-Ting Ho, Tien-Lu Huang, Yue Tan, Cissel Tan, Min Zhou, Zhi Qiu, and many others. I thank them for being there with me during those wonderful and not-so-wonderful times in graduate school.

Finally, and most importantly, I would like to thank my parents and my dear sister. Without their unconditional love and support, I wouldn't have gone this far.

Vita

2004.....B.Sc. Physics, National Tsing Hua University, Hsinchu, Taiwan

2006.....M.Sc. Physics, National Tsing Hua University, Hsinchu, Taiwan

2008 to present.....Graduate Teaching and Research Associate, The Ohio State University, Columbus OH

Publications

- Yu-Sheng Ou, **Yi-Hsin Chiu**, N.J. Harmon, Pat Odenthal, R. K. Kawakami, M.E. Flatté, E. Johnston-Halperin, "Exchange-driven spin relaxation in ferromagnet/oxide /semiconductor heterostructure", submitted to Physical Review Letters

- **Yi-Hsin Chiu,** Nicholas G. Minutillo, Robert E. A. Williams, Greg J. Smith, David W. McComb, John A. Carlin, E. Johnston-Halperin, Fengyuan Yang, "Photoluminescence and Morphology Evolution in GaAs/AlGaAs Core/Shell Nanowires Grown by MOCVD: Effects of Core Growth Temperature", accepted by Journal of Crystal Growth.

- Lei Fang, Xianwei Zhao, **Yi-Hsin Chiu**, Dongkyun Ko, Kongara M. Reddy, Thomas R. Lemberger, Nitin P. Padture, Fengyuan Yang, and E. Johnston-Halperin, "Comprehensive control of optical polarization anisotropy in semiconducting nanowires", *Appl. Phys. Lett.* **99**, 141101 (2011)

Fields of Study

Major Field: Physics

Table of Contents

List of Figures

Chapter 1: Introduction and background

1.1 Motivation

Spin is an intrinsic form of angular momentum that elemental particles possess. While conventional electronics utilize the charge degree of freedom to realize device functionalities, "spintronics" aims to make use of the spin degree of freedom. In principle, manipulation of spins is faster, consumes less power, and takes smaller space, making spintronics a promising alternative to electronic technology[1,2].

To date, metal spintronics has had great success in the information (IT) industry such as modern hard disk drives based on giant magnetoresistance effect (GMR) and magnetic random access memory (MRAM)[2]. The operational principle relies on reorienting magnetic domains relative to a reference, such as a magnetic field or the magnetization orientation of a ferromagnet. Semiconductor spintronics, on the other hand, has yet to fulfill its full potential. Incorporating spins in semiconductors requires the following essential capabilities: (i) injection of spins, which means the creation of a non-equilibrium spin polarization in semiconductors, (ii) manipulation of spins, which requires appropriate spin coupling that simultaneously allows for long spin lifetime and fast manipulation, and (iii) sensitive detection of spin coherence[3,4].

The solutions to these challenges lie in a deeper understanding of spin interactions and spin relaxation in semiconductors as well as appropriate tools to probe spin dynamics. In particular, recent experiments have suggested the important role of dimensionality on spin dynamics. For example, spin-orbit interaction, the dominant source of spin relaxation in most II-VI and III-V semiconductors, has been shown to be significantly suppressed in reduced dimensions[5–7]. Low-dimensional semiconductors are therefore appealing candidates for exploring spin physics and device applications.

This dissertation aims at exploring spin dynamics in low dimensional semiconductor systems using time-resolved optical techniques. The time resolution provided by this technique allows for a direct measurement of the equilibrium and non-equilibrium carrier spin as well as various spin interactions in the time domain[8]. Optical approaches are also a natural fit for probing optically active nanostructures[1,9], where electric approaches can often encounter challenges. For instance, fabricating electric contacts with nanostructures is an proven challenge because of their small size and modified electronic structure[10].

This dissertation is divided into three sections targeting an ultimate goal of employing optical methods to explore spin dynamics in low dimensional semiconductors. First, the time-resolved Kerr rotation technique is employed to study spin relaxation in Fe/MgO/GaAs heterostructures. The results reveal rich interactions between the GaAs nuclear spins, electron spins, and the neighboring Fe spins, as well as the resulting exchange-driven electron spin relaxation in GaAs. This lays the groundwork for this dissertation to explore low dimensional systems.

Second, we work to facilitate optical studies of spin dynamics in one dimension (1D), which hasn't been possible in the past due to the fundamental challenge of optical polarization anisotropy. We propose a dielectric-matched membrane structure based on GaAs/AlGaAs core-shell nanowires. By simultaneously addressing the optical polarization anisotropy and various technical challenges, this study offers a promising route to optical investigations of 1D spin physics.

Third, a novel 2D material, germanane (GeH), is investigated by continuous wave (cw) polarization-resolved photoluminescence (PL) spectroscopy as a first step toward future ultrafast pump-probe study. PL develops a finite degree of circular polarization under circular excitation (optical orientation) or in an applied magnetic field (Zeeman effect), indicating the presence of spin-polarized carriers. This study presents the first magneto-optical investigation in germanane.

1.2 Organization of the chapters

The chapters are organized as follows. In chapter 1, spin physics in semiconductors is reviewed, primarily focusing on spin interactions and spin relaxation mechanism. Chapter 2 describes the optical techniques employed in this dissertation, namely, time-resolved Kerr rotation spectroscopy, continuous wave (cw) polarization-resolved photoluminescence spectroscopy, and optical orientation. The basic physical principle and the experimental implementation are discussed. Chapter 3 presents the study of the exchange-driven spin relaxation in Fe/MgO/GaAs heterostructure. Chapter 4 discusses the work on realizing all-optical approaches to probing spin dynamics in 1D. Chapter 5 presents the studies of magneto-optical interactions and optical orientation in germanane.

1.3 Spin physics in semiconductors

1.3.1 What is spin?

Spin is an intrinsic form of angular momentum possessed by elementary particles, composite particles, and atomic nuclei. It is a purely quantum mechanical property without a classical analogy. Discovered in the 1920's in the fine structure of hydrogen spectral line and the Stern-Gerlach experiment[11], electron spin has a quantum number S =1/2, with the angular momentum

$$S = \sqrt{S(S+1)}\hbar = \frac{\sqrt{3}}{2}\hbar \tag{1.1}$$

where $\hbar$ is the reduced Planck constant. $\hbar = \frac{h}{2\pi}$, and h is the Planck constant. The z-component of the angular momentum S_Z takes two values,

$$S_z = \pm\frac{1}{2}\hbar \tag{1.2}$$

typically referred to as a "spin-up" and "spin down" state. Associated with the spin angular momentum is a magnetic moment. The z-component of this magnetic moment of an electron spin is usually expressed as a multiple of the Bohr magneton,

$$\mu_Z = \pm\frac{1}{2}g\mu_B \tag{1.3}$$

where μ_B is the Bohr magneton

$$\mu_B = \frac{e\hbar}{2m_e} = 9.2740154 \times 10^{-24}\text{J/T} = 5.7883826\times\frac{10^{-5}eV}{T} \tag{1.4}$$

and g is the gyromagnetic ratio, or commonly known as the g factor. For a free electron, g =2.0023. In solid states systems, the g factor can vary depending on the fundamental interactions present in the system. For instance, bulk GaAs has an electron g factor of -0.44.

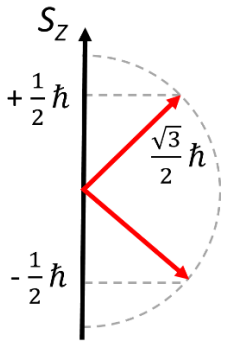

Fig 1.1 A classical picture of electron spin. The projection along z direction shows the two quantum states, "spin-up" and "spin down", corresponding to $S_z = +1/2\hbar$ and $-1/2\hbar$.

Spins interact with magnetic fields. In a transverse magnetic field, a spin precess at Larmor frequency ω_L. For an electron spin, the Larmor frequency is given by $\omega_L = eB/2m_e$, where e is the electron charge, B the magnetic field, and m_e the electron mass. In a longitudinal magnetic field, Zeeman effect leads to a spin-dependent interaction energy, called Zeeman energy, $E_{Zeeman} = -g\mu_B SB$. Due to the small Bohr magneton ($\mu_B = e\hbar/2m_e = 5\times10^{-5}$ eV/T), electron Zeeman energy is usually quite small compared to other interactions in the solid state systems. As a consequence, an electron spin only couples weakly to its magnetic environment.

1.3.2 Spin interactions

This section reviews the spin interactions that are relevant to the focus of this dissertation. For a complete review, see Ref [12].

Pauli exclusion principle

Being a spin ½ system, electrons are fermions and are constrained by the Pauli exclusion principle, which requires that no two electrons can occupy an identical quantum state. Although the Pauli exclusion principle doesn't involve any interaction, it is a manifestation of the electron spin and is at the very core of the structure of atoms, governing various physical and chemical properties in condensed matter systems.

Exchange interaction

Exchange interaction is a quantum effect between identical particles. The spin dependence results from Pauli exclusion principle. Due to the Pauli exclusion principle and the indistinguishability of individual electrons, the wave function of a pair of electrons needs be anti-symmetric upon the exchange of the two electrons, leading to a spin-dependent energy. The exchange Hamiltonian of two electrons can be expressed as

$$H = -2J_{ij}\boldsymbol{S}_i \cdot \boldsymbol{S}_j \tag{1.5}$$

Where $\boldsymbol{S}_i$ and $\boldsymbol{S}_i$ are the individual spin, and J_{ij} is the exchange integral, describing the strength of the interaction. When J_{ij} is positive, exchange interaction leads to an alignment of the spins because it is energetically favorable. This is the origin of ferromagnetism. When J_{ij} is negative, exchange interaction leads to ferrimagnetism and antiferromagnetism.

Exchange interaction is usually negligible in semiconductors, but plays an essential role in magnetic semiconductors[13,14] and ferromagnet/semiconductor heterostructure[15,16]. The study of exchange coupling at ferromagnet/semiconductor interface is in fact one of the most important topics in spintronics[3,4].

Spin–orbit interaction

Spin-orbit interaction is an interaction that couples the spin of a particle with its orbital motion. It is a consequence of a charged particle moving in an electric field. For an electron in solid state system moving with velocity $\boldsymbol{v}$, the electric field $\boldsymbol{E}$ from the nuclei creates an effective magnetic field $\boldsymbol{B} = (\boldsymbol{v}/c) \times \boldsymbol{E}$. This effective internal field, or Spin-orbit field, can be intuitively understood by going to the electron's rest frame. In the rest frame of the electron, the electron sees the nucleus moving around it, generating an electric current and therefore a magnetic field acting on the electron spin. The spin-orbit Hamiltonian can be written as

$$H_{so} = A\boldsymbol{L} \cdot \boldsymbol{S} \tag{1.6}$$

Where $\boldsymbol{L}$ and $\boldsymbol{S}$ are the orbital and spin angular momentum of the electron, and the constant A depends on the electron state in an atom.

In order for spin-orbit interaction to occur, there must be a certain asymmetry in the system. For a symmetric crystal, the electric field from the nuclei will be averaged out and no spin-orbit interaction occurs. Spin-orbit interaction increases for heavier atoms because of the enhanced electric field produced by the nuclear charge $+Ze$ when Z increases (Z is the atomic number).

In III-V and II-VI semiconductors, spin-orbit interaction is often the dominant source of spin relaxation[3,4]. Spin-orbit interaction provides an indirect channel to access the spin degree of freedom of an electron, allowing for manipulation of spin states by electric means. It is also the existence of the spin-orbit interaction that enables optical spin orientation and detection.

Hyperfine interaction with lattice nuclei

Hyperfine interaction is an interaction between the electron and nuclear spins, also known as Fermi contact interaction. The Hamiltonian describing this interaction is given by[17]

$$\mathcal{H}_{HF} = \sum_{k=1toN} A_k \vec{I}_k \vec{S} \tag{1.7}$$

Where $\overrightarrow{I_k}$ and $\vec{S}$ are the spin operator for nucleus k and the electron spin, respectively. A_k is the coupling strength between each nuclear spin k and the electron spin. The coupling strength between the electron spin and the nuclear spin varies for each nuclear spin because the electron wave function is inhomogeneous. A_k is proportional to the probability density of the electron at the location of the nucleus. Therefore, the hyperfine interaction is important for an electron in the s orbital, but is zero for a p-state electron. For the same reason, hyperfine interaction is more effective when the electrons are localized. For example, electrons bound to a donor experience a much stronger hyperfine interaction with nuclear spins compared to iterant electrons.

An important feature of hyperfine interaction is that it is essentially a many-body quantum mechanical behavior. While the nuclear spins affect the electron spin dynamics, the electron spin also has an impact on the dynamics of each of the nuclear spins. The coupling between them can be quite complex. A semiclassical description of the nuclear spins is to treat them as an effective magnetic field, called Overhauser field. Overhauser field B_N represents the response of the ensemble of nuclear spins

$$\left(\sum_{k=1toN} A_k \vec{I}_k\right)\vec{S} = g\mu_B B_N \vec{S} \tag{1.8}$$

The coupling of the electron spins to the nuclear spins can then be simplified as an electron spin in an external magnetic field B_N [18].

Hyperfine interaction between the electron spins and nuclear spins provides an effective approach to polarizing nuclear spins. In the process of dynamic nuclear polarization (DNP), where non-equilibrium electron spins interact with nuclear spins via hyperfine interaction and hyperpolarize the nuclear spins, the nuclear polarization can increase up to 50 %. This is in strong contrast with the magnetic field induced nuclear polarization, which is typically around 1% or less.

1.3.3 Spin lifetimes

Spin lifetime is the characteristic time that spin loses its coherence. Decoherence of spin can occur in two ways: spin relaxation and spin dephasing. Traditionally, spin dynamics are described within the framework of the Bloch-Torrey equations for magnetization dynamics[19].

$$\frac{dM_x}{dt} = \gamma(\boldsymbol{M} \times \boldsymbol{B})_x - \frac{M_x}{T_2}$$

$$\frac{dM_y}{dt} = \gamma(\boldsymbol{M} \times \boldsymbol{B})_y - \frac{M_y}{T_2}$$

$$\frac{dM_z}{dt} = \gamma(\boldsymbol{M} \times \boldsymbol{B})_z - \frac{M_z - M_0}{T_1} \tag{1.9}$$

Where $\gamma = \mu_B g/\hbar$ is the electron gyromagnetic ratio, and $M_Z^0 = \chi B$ is the thermal equilibrium magnetization with χ denoting the system's static susceptibility. Since a spin has an associated magnet moment, one can relate a spin with the magnetization induced by the spin magnetic moment. The two phenomenological time constants T_1 and T_2 in the

Bloch-Torrey equations then represent the spin lifetimes characterizing spin dynamics in an applied magnetic field.

T_1 is known as the longitudinal relaxation time. As shown in the Bloch-Torrey equations, T_1 represents the characteristic time for the longitudinal magnetization component to reach equilibrium (aligned with the external magnetic field). For spin dynamics, it is associated with the relaxation of the average spin polarization toward thermal equilibrium through a transition between the spin-up and spin-down states. This process is usually inelastic and involves energy absorption or emission with the environment. For instance, the lattice bath, or phonon, can participate in the energy exchange to dissipate the spin-flip energy. For this reason, T_1 is also referred to as the spin-lattice relaxation time.

The other parameter, T_2, is called transverse relaxation time or dephasing time. A quantum spin is in a superposition state of spin "up" and spin "down" with well-defined phase. With the environmental interactions, the phase coherence can be destroyed. T_2 describes the corruption of phase coherence of the transverse component of a single spin, or an ensemble of spins that are initially precessing in phase.

Loss of phase coherence can be reversible or irreversible. While T_2 is reserved for processes with irreversible phase loss, another parameter T_2^*, describe the characteristic time for an ensemble of spins to loss its phase coherence when there is reversible dephasing on top of the irreversible processes, which is normally the case. Reversible dephasing is often associated with inhomogenous precession frequency among the ensemble spins. The inhomogeneity can arise from an inhomogeneous external magnetic field, the inherent *g*-

factor variation between different orbital states, or simply the material inhomogeneity. Spin echo experiments have successfully demonstrated the elimination of the reversible dephasing by applying a 180º pulse[20]. In general, $T_2^* \leq T_2$, meaning that the macroscopic ensemble response can lose its coherence (T_2^*) while the coherence on the individual spin level is still retained (T_2).

1.3.4 Spin relaxation mechanism

Since the discovery of the long spin relaxation time of itinerant electrons up to 100 nanoseconds and spin diffusion length over 100 μm in GaAs[21], extraordinary advances have been made to understand how spin relaxes. In semiconductors, the most important mechanisms include Elliott-Yafet, D'yakonov-Perel', Bir-Aronov-Pikus, and hyperfine interaction processes. We'll focus on the DP mechanism and the hyperfine interaction for their relevance to this dissertation. For a complete review, see Ref [3].

D'yakonov-Perel' mechanism

D'yakonov-Perel' (DP) Mechanism[22–24] arises from spin-orbit interaction in crystals lacking inversion symmetry. The asymmetry in the crystal structure causes incomplete cancelation of the electric field from the nuclei of the host lattice and leads to an internal electric field that is essential for spin-orbit interaction to occur. The spin-orbit field (the effective magnetic field produced by spin-orbit interaction) due to DP mechanism depends on the value of the electron k-vector and its direction with respect to the crystal axes.

The way spin decays via the DP mechanism is illustrated in Fig. 1.2. Since the spin-orbit field is k dependent, it stays constant between the scattering events and changes its orientation and magnitude when the electron scatters. Consequently, momentum scattering due to collisions with impurities or phonons leads to fluctuations in the effective magnetic field that the electron spin sees. This scattering-induced fluctuation in the effective magnetic field is the source of spin decoherence.

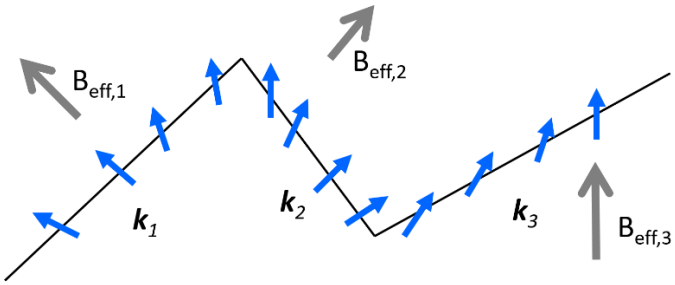

Fig 1.2 Illustration of the spin relaxation process due to DP mechanism. The electron spin (blue arrows) precesses around an effective magnetic field generated by spin-orbit interaction (grey arrows) that is dependent on the electron k-vector. Fluctuation in the effective magnetic field occurs upon momentum scattering events and gives rise to the suppression of the spin coherence.

The resulting spin dephasing depends on the strength of the effective field and the frequency of the scattering events. In the normal condition, the scattering events are very frequent. If we define Ω to be the spin precession frequency in this field and τ_P to be the momentum scattering time, $\Omega\ \tau_P$ is usually very small. The spin lifetime τ_s and the momentum scattering time τ_p follow the following relation.

$$\frac{1}{\tau_s} \sim \Omega^2 \tau_P \tag{1.10}$$

One can see from equation (1.11) that the spin lifetime gets longer when the scattering intensity increases (shorter τ_p). This is an important feature of DP spin relaxation

and can be understood by the "motional narrowing" effect. In this regime where $\Omega \tau_P \ll 1$, the momentum scattering rate is sufficiently intense such that the phase change between two scattering events is tiny. As a result, increased scattering intensity does not destroy the spin coherence but helps to establish a random-walk-like fluctuation of the phase, leading to an enhancement of the spin lifetime.

Relaxation via hyperfine interaction

Hyperfine interaction is the interaction between electron spin and nuclear spin. Via hyperfine interaction, the fluctuations in nuclear spins can affect electron spin dynamics and cause spin decoherence.

Utilizing the concept of Overhauser field, the interaction between electron spin and nuclear spins can be considered as a modification to the magnetic field the electron spin experiences. The total magnetic field can be written as $\boldsymbol{B}_{tot} = \boldsymbol{B}_{ext} + \boldsymbol{B}_N$ (vector sum), where $\boldsymbol{B}_{tot}$ and $\boldsymbol{B}_{ext}$ are the total magnetic field and the applied external field, respectively.

Without any fluctuation in the nuclear field (constant field in time), the Overhauser field only makes a correction to the total magnetic field. The electron spin now precesses in a constant $\boldsymbol{B}_{tot}$ (not $\boldsymbol{B}_{ext}$) and the electron spin maintains its coherence. It is when there are fluctuations in the nuclear field (either temporally or spatially) that the electron spin relaxation occurs. In this case, the electron spin experiences a time-varying $\boldsymbol{B}_{tot}$ and precesses around a time-varying axis with a time-varying frequency. As a result, the spin coherence is lost.

The fluctuation in Overhauser field could come from changes in the local nuclear polarization through dynamic nuclear polarization or inhomogenous doping concentration. It could also arise from the flip-flop of two nuclei. In the latter case, the total nuclear polarization remains constant. The Overhauser field changes because the coupling strength between each nuclear spin k and the electron spin is different, resulting in changes in $\sum A_k \vec{I}_k$.

1.3.5 Coupling between spin and light

The intimate relation between carrier spin and circularly polarized light is of central importance for optically accessing spins. It forms the basis for the optical excitation and detection of spin polarization.

In most III-V and II-VI semiconductors, coupling between the spin polarization and circular polarization of light lie in the optical selection rules and spin-orbit interaction. To review this effect, we consider bulk GaAs under the excitation of circularly polarized light. Fig. 1.3 shows the band structure of GaAs near the Γ point of the Brillouin zone. The conduction bad is s-like, with the total angular momentum quantum number J=1/2, and the projection of the total angular momentum J_z=±1/2. The valence band consists of a degenerate heavy hole (HH) and light hole (LH) band, with J=3/2, and J_z=±3/2 for heavy hole states, J_z=±1/2 for light hole states, and a split-off band with J=1/2 due to the spin-orbit interaction. The band gap, E_g, is 1.52 eV and the energy separation between the split-off band and the HH and LH band, Δ, is 0.34 eV[17].

For an optical transition to occur, optical selection rules require that the angular momentum to be conserved. Consequently, when a circularly polarized photon is absorbed, the angular momentum it carriers ($\hbar$ or - $\hbar$, depending on the helicity of the photon) is distributed between the photo-excited electron and hole.

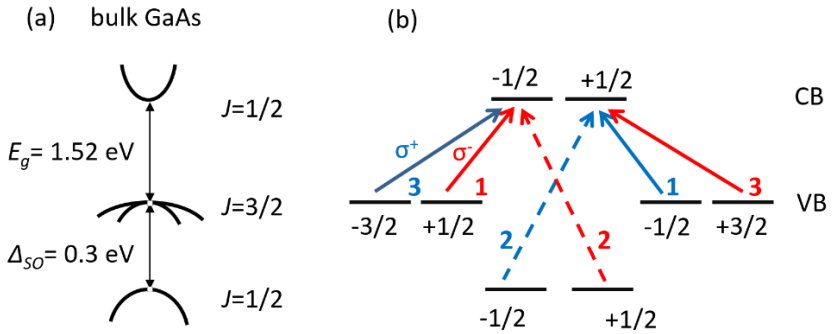

Fig 1.3 (a) Cartoon of the band structure of bulk GaAs (b) Optical transitions under σ^+ excitation (blue arrows) and σ^- excitation (red arrows) excitation and the corresponding transition probabilities (heavy hold: light hole: split-off hole = 3:1:2).

For a photon with angular momentum $\hbar$ (σ^+ excitation) and energy $E = \underline{E_g}$ (resonant excitation), optical selection rules require that only transitions with Δm=+1 occur, i.e. transitions from J_z=-3/2 HH state to J_z=-1/2 electron state, and from J_z=-1/2 LH state to J_z=+1/2 electron state (blue arrows in Fig. 1.3 (b)). Furthermore, the ratio of transition probability for the HH and LH transitions is 3:1. Consequently, a 1:3 population imbalance of photo-excited spin-up and spin down electron arises in the conduction band, while a complete orientation takes place in the valence band where all the photo-excited holes are spin-up. Alternatively, one can selectively populate the spin-down states in the conduction band with σ^- excitation (red arrows in Fig. 1.3 (b)).

It is important to recognize the crucial role of spin-orbit interaction here. While the helicity of the photons select the possible transitions between the orbital states, it is the spin-orbit interaction that determines the preferential spin population. If we were to turn off the spin-orbit interaction in GaAs, the split-off band would become degenerate with the HH and LH bands and participate in the optical process (dashed arrows in Fig. 1.3 (b)). As a result, the spin polarization becomes zero even under a circular excitation.

The optical selection rules that govern the excitation process also apply to the emission process. One can expect a nonzero degree of circular polarization in the luminescence to occur when there is a net carrier spin. This is the underlying mechanism for optical detection of the carrier spin polarization using the circular polarization of luminescence.

The actual relation between the carrier spin and circular polarization of light is usually more complex than what we described above. Spin relaxation and various other effects can come into play. Nevertheless, optical selection rules and spin orbit interaction form the fundamental basis of the coupling between the carrier spins and the light. More detailed discussion of the optical orientation and the luminescence-based detection of carrier spins will be presented in Chapter 2.

Chapter 2: Optics as a probe for spin dynamics

The intimate relation between carrier spin and circularly polarized light enables optical investigation of spin dynamics. (For more detail, see Section 1.2.5) In this chapter, we review the optical techniques employed in this dissertation, namely, time-resolved Kerr rotation spectroscopy, continuous wave (cw) polarization-resolved photoluminescence spectroscopy, and optical orientation.

2.1 Optical orientation

Optical orientation is the process where spin-oriented carriers are created in a material through the interband absorption of circularly polarized photons[17]. To date, optical orientation remains the most effective method for establishing spin polarization. Depending on the conduction-band and valence-band states participating in the optical transitions, a spin polarization close to 100 % (full spin alignment of carriers) can be achieved[25].

Optical orientation relies on the optical selection rules and the presence of the spin orbit interaction, which have been discussed in Section 1.2.5. In the following discussions, we will focus on the steady-state spin polarization and the relevant factors that impact the degree of spin orientation.

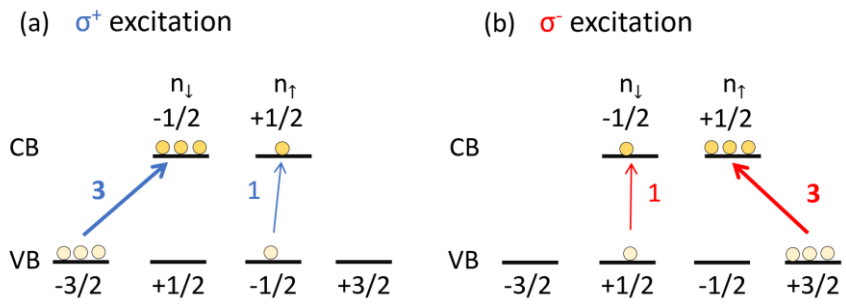

Fig 2.1 Photo-carrier distribution in GaAs upon σ^+ (a) and σ^- (b) excitation. Optical selection rules allow only the transitions indicated by the blue/red arrows to take place upon the σ^+/ σ^- excitation, respectively. The relative transition probably between the HH and LH state is 3:1. Thus, circular excitation creates a spin orientation both in the conduction band and the valence band, depending on the excitation helicity. The excitation energy is chosen such that no transitions from split-off band occurs.

Fig. 2.1(a) shows the carrier distribution upon σ^+ circular excitation. An initial spin orientation is established in both the conduction band (with a population imbalance of 1:3 between the spin-up and spin-down electron) and the valence band (all spin-up). Two important clarifications need be made here. First, the orientation of the photo-excited carriers described above is only one of the two factors that determines the initialized spin polarization. Since practically all semiconductors are doped either intentionally or unintentionally, one has to take into account the presence of the un-oriented equilibrium carriers when calculating the spin polarization. Depending on the doping type, the contribution of the equilibrium carriers can be important or negligible.

Second, the initialized spin polarization represents the initial spin polarization at the instant of creation and may differ from the steady-state value. The difference primarily originates from spin relaxation and carrier recombination.

Next, we discuss the steady-state spin polarization in p-type and n-type GaAs and demonstrate the central role of equilibrium carriers, spin relaxation, and carrier combination in the optical orientation process.

Steady-state orientation in p-type GaAs

First of all, in either p-type or n-type GaAs, the hole orientation initialized by the optical orientation is quickly lost due to the mixing of the HH and LH band[17], typically on the time scale of ps. Hence, hole spin polarization practically doesn't occur. On other hand, the electron spin polarization can be achieved and the steady-state value depends on the doping type.

As discussed earlier, the ratio between spin-up and spin-down population of the photo-excited electrons is 1:3 upon the σ^+ excitation. In p-type GaAs, the spin polarization is entirely determined by the oriented photo-electrons as there is no equilibrium carriers present in the conduction band (considering the zero temperature limit). Therefore, optical orientation gives rise to an initial spin polarization P_0 of -50 %. Here, the spin polarization is defined as

$$P = \frac{N_\uparrow - N_\downarrow}{N_\uparrow + N_\downarrow} \tag{2.1}$$

where $N_\uparrow$ and $N_\downarrow$ are the number density of the spin-up and spin-down carrier, respectively. The negative sign of P_0 indicates that the optically-oriented electrons have a net polarization anti-parallel to the direction of the angular momentum of the exciting photon. Alternatively, one can look at the average spin at the instant of creation, S_0. σ^+ excitation creates an S_0. of -0.25, given by (+1/2)×((1/4)+(-1/2) × (3/4). Again, the negative sign is

an indication of the opposite alignment between the resulting electron spin polarization and the photon angular momentum. Similarly, an initial electron polarization of 50 % and an initial average spin of 0.25 will be generated when the helicity of the excitation is switched to σ^- polarization (Fig. 2.1 (b)).

This optical orientation process is sometimes referred to as *optical spin pumping*, where the minority carriers become oriented. An important feature of optical spin pumping is that the resulting spin polarization is independent of the strength of the optical excitation, The excitation strength changes the number of oriented electrons (hence, the average spin *S*) but not the relative population ratio between the spin-up and spin-down electrons (hence, the spin polarization *P*). In the following discussion, we will focus our attention on the average spin *S*.

From the initialization of S_0, the evolution of *S* depends on the spin relaxation. When the spin lifetime is much longer than the carrier recombination time, which is normally the case in most semiconductors, non-equilibrium carriers retain their spin memory when they recombine, making the steady-state *S* equal to its initial value. In the opposite case when the spin lifetime is much shorter than the recombination time, the spin polarization is quickly destroyed. The general behavior of the steady-state *S* can be described by the following formula,

$$S = \frac{S_0}{1+\tau/\tau_s} \tag{2.2}$$

where τ is the carrier recombination time and τ_s is the spin relaxation time. The ratio τ/τ_s fundamentally determines the average spin created by the optical orientation.

Steady-state orientation in n-type GaAs

In n-type semiconductors, optical orientation leads to an orientation of the majority carriers, often referring to as *optical spin orientation.* In this case, optical orientation generates oriented electron into the conduction band where non-oriented equilibrium electrons are present. Since the recombination process does not distinguish between the two, the optical excitation essentially replaces the non-oriented equilibrium electrons with the oriented photo-excited electrons. In the absence of spin relaxation, stationary excitation would establish a complete orientation of the electron spins. The presence of spin relaxation imposes a limit on the degree of orientation. The resulting average electron spin is therefore determined by the balance between the electron-hole generation rate G and the spin relaxation rate $1/\tau_s$.

$$S = \frac{S_0}{1+\tau_e/\tau_s} \tag{2.3}$$

Here τ_e is the lifetime of an electron in the conduction band. S_0 is the initialized average spin of the photo-excited electrons at the instant of creation and is equal to -0.25 or +0.25 under σ^+ or σ^- excitation, respectively, for bulk GaAs. In the steady state, the requirement that the recombination rate to be equal to the photoexcitation rate yields,

$$\frac{n}{\tau_e} = G \tag{2.4}$$

,where *n* is the electron concentration. Substituting Eq. (2.4) into (2.3) gives,

$$S = \frac{S_0}{1+n/G\tau_s} \tag{2.5}$$

The average spin now has an excitation power dependence. At small excitation intensity, $G\tau_s$ <<n, the average spin is proportional to the excitation power ($S \sim S_0\, G\tau_s /n$). It grows with the increase of excitation power until reaching the saturating value of S_o.

2.2 Steady-state spectroscopic optics: Photoluminescence

Photoluminescence (PL) spectroscopy is a technique widely used to study semiconductors and alloys. Useful information such as the optical band gap and the carrier effective mass can be extracted through the analysis of the luminescence. It is also a powerful tool to probe shallow impurities, structure disorders, and non-radiative recombination centers. Of particular interest to the focus of this dissertation is its spintronic capability. The coupling between the electron spins and the circular polarization of light allows for spin detection using the circular polarization of the PL

In the following sections, we first review the photoluminescence spectroscopy in order to provide prerequisite knowledge of the operating principles and essential concepts in the PL process. We then discuss the polarization-resolved PL experiments and the information it can yield about the spin state.

2.2.1 Photoluminescence spectroscopy

The photoluminescence process involves three critical steps, as shown in Fig. 2.2 (a). First, a photon with energy E_0 comes in and excites an electron from the valence band to the conduction band, creating an electron-hole pair (blue arrow in Fig. 2.2 (a)). Energy conservation requires that the energy separation of the resulting electron and hole to be equal to the energy of the absorbed photon, E_0. In addition, due to the relatively small momentum associated with photons, this optical transition is almost vertical, meaning that no momentum change is involved.

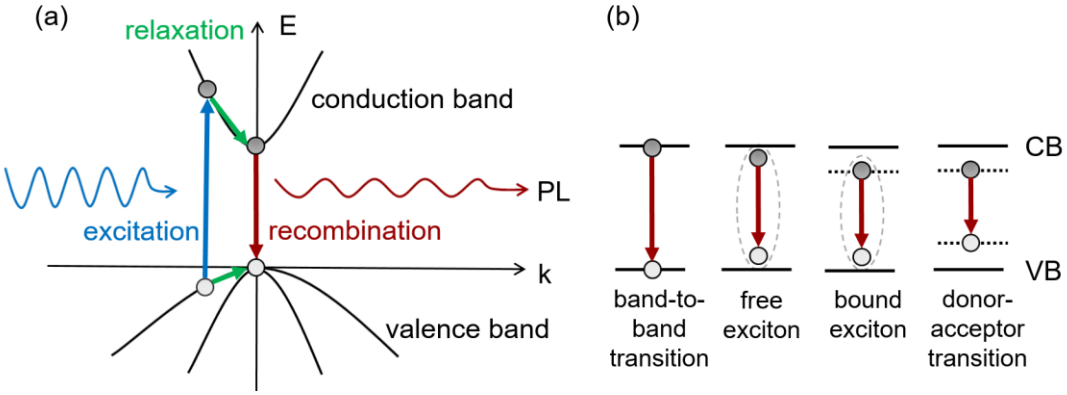

Fig 2.2 (a) Three critical steps involved in the photoluminescence process: excitation (blue arrow), relaxation (green arrows), and recombination (red arrow). (b) Recombination processes commonly observed in the PL: band-to-band transition, free exciton, exciton bound to donors, and donor-acceptor transition. The black dashed lines represent the donor and acceptor states. The grey dashed curves indicate the Coulomb interaction between the electron-hole pair.

Once the carriers are excited, they undergo thermal relaxation processes, mostly via the interaction with acoustic or optical phonons (green arrows in Fig. 2.2 (a)) Thermal relaxation in most III-V and II-VI semiconductors happens very fast (on the time scale of ps) compared to the recombination time (~ns). Therefore, an accumulation of energy-relaxed carriers soon develops near the band edge (the bottom of the conduction band for electrons and the top of the valence band for holes) before the recombination takes place. It is the recombination between these near-band-edge states that then contribute to the photoluminescence (red arrow in Fig. 2.2 (a)). Fig. 2.2 (b) illustrates the recombination processes commonly observed in the PL. In most cases, the created electron and hole form a Coulomb-attracted pair, known as an exciton. Free excitons have an energy smaller than the band gap due to the Coulomb interaction. Excitons can also be Coulomb-bounded by

donors or acceptors, forming bound excitons. Alternatively, transitions can occur between the donor and acceptor states. The band-edge sensitivity of PL makes it a powerful tool to study the optical band gap and shallow defect states near the band edge, both are of fundamental importance for semiconductor research.

The schematic of the PL setup used in this dissertation is shown in Fig. 2.3 (a).

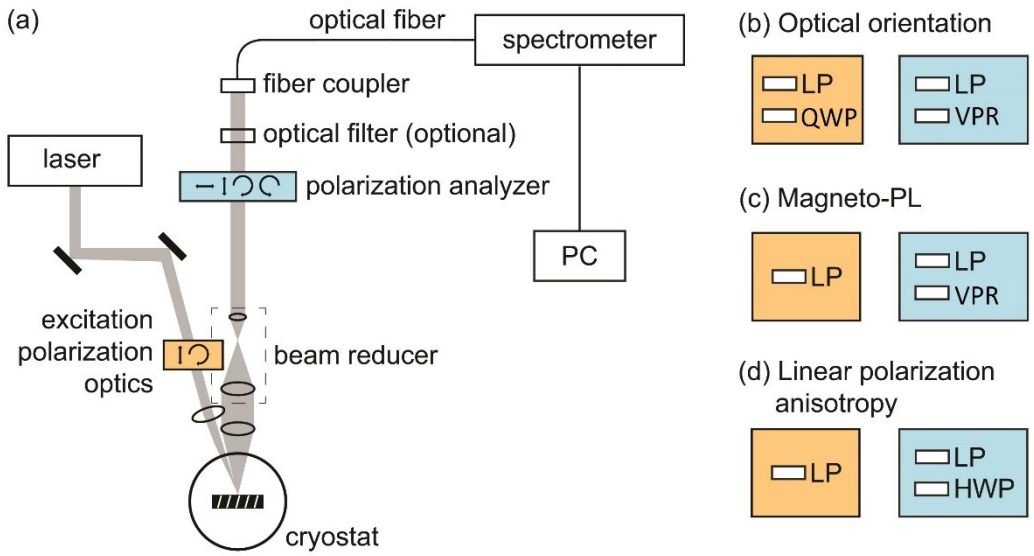

Fig 2.3 (a) Schematic of the polarization-resolved PL setup. (b)-(d) Polarization optics used for excitation (left panel) and detection (right panel) for optical orientation (b), magneto-PL (c), and linear polarization anisotropy (d) experiments. Here, LP stands for linear polarizer. QWP stands for quarter waveplate. HWP stands for half waveplate. VPR stands for variable phase retarder.

A Nd:YVO_4 or helium-neon continuous-wave laser is used to excite the sample under study. The laser beam is directed into an optical cryostat (Oxford Instruments, Spectromag) with an incident angle of less than 10 º with respect to the surface normal of the sample. A lens of focal lens of 20 cm is used to focus the excitation beam onto the

sample with a spot size of ~ 50 μm. The luminescence is collected in the normal direction, using a lens of focal lens of 15 cm. The collimated PL beam after the collection lens goes through a beam reducer, which consists of a pair of lens with the focal lens of 10 cm and 2.54 cm to reduce the size of the PL beam for efficient coupling to the optical fiber. A fiber coupler (a 20× objective lens in our case) then focuses the PL beam into an optical fiber, which transmits the PL to a 0.3 m spectrometer (PI-Acton, SpectraPro-2300i) and a liquid N_2 cooled CCD camera (Spec-10) for spectrally-resolved intensity measurement. Optical filters are often placed before the fiber coupler to eliminate excitation contamination or unwanted stray lights in the PL detection.

This setup can be modified to perform polarization-resolved PL experiments by including polarization optics in the beam path, as will be discussed in Section 2.2.2.

2.2.2 Polarization-resolved photoluminescence

Spin detection using the circular polarization of the PL has been a well-established technique commonly used in the studies of the optical orientation and electric spin injection[3]. Furthermore, the evolution of the circular polarization in a transverse external field provides information about the spin relaxation and measures the spin lifetime T_2* (Hanle effect)[3,17].

The connection between the degree of circular polarization of the PL and the carrier spin polarization rely on the optical selection rules (as discussed in Section 1.2.5). For the case of bulk GaAs, considering the spin polarization in the conduction band is $P_{spin} =$

$\frac{n_\uparrow - n_\downarrow}{n_\uparrow + n_\downarrow}$ ($n_\uparrow$ and $n_\downarrow$ are the number of spin-up and spin-down electrons, respectively), the detected circular polarization $P_{circ} = \frac{I_{\sigma^+} - I_{\sigma^-}}{I_{\sigma^+} + I_{\sigma^-}}$ can be written in terms of $n_\uparrow$ and $n_\downarrow$ as $P_{circ} = \frac{I_{\sigma^+} - I_{\sigma^-}}{I_{\sigma^+} + I_{\sigma^-}} = \frac{(n_\downarrow + 3n_\uparrow) - (3n_\downarrow + n_\uparrow)}{(n_\downarrow + 3n_\uparrow) + (3n_\downarrow + n_\uparrow)} = \frac{1}{2}\frac{n_\uparrow - n_\downarrow}{n_\uparrow + n_\downarrow} = 0.5\, P_{spin}$. Therefore, the resulting circular polarization of the PL is 50 % of the spin polarization. The conversion ratio between P_{circ} and P_{spin} is closely linked to the degeneracy of the HH and LH states. Higher conversion ratio can be achieved when this degeneracy is lifted by the spatial confinement. For instance, $P_{circ} = (\pm) P_{spin}$ in quantum wells[17].

In addition to the detection of the spin polarization, the circular polarization of the PL in the presence of a longitudinal magnetic field yields information about the magneto-optical interactions. In this case, Zeeman effect lifts the spin degeneracy, leading to an energy splitting $\Delta E = = -g\mu_B m_J B$ (Section 1.3.1). Since the occupation probability of the electronic states is given by the Boltzman distribution, Zeeman splitting of the spin states results in a spin polarization. The circular polarization of the PL then measures this field-induced spin polarization.

The measurement of the circular polarization (CP) is carried out by measuring the PL intensity of the σ^+- and σ^-- polarized component, yielding a circular polarization CP $= \frac{I_{\sigma^+} - I_{\sigma^-}}{I_{\sigma^+} + I_{\sigma^-}}$. In order to improve the signal-to-noise ratio, the CP measurement is usually repeated multiple times and an averaged CP spectrum is reported.

Fig. 2.3 (b) shows the polarization optics used in the polarization-resolved experiments. The polarization state of a circular excitation (for the optical orientation experiments) is prepared by a Glan-Laser linear polarizer (LP) and a calibrated quarter

waveplate (QWP) to allow for σ^+- and σ^--polarized excitation. The analysis of the circular polarization of the luminescence (for the optical orientation and magneto-PL experiments) is realized by using a liquid crystal variable phase retarder (VPR) and a Glan-Thompson linear polarizer. To perform the optical polarization anisotropy experiments, the excitation polarization is kept constant at the *S* polarization using a Glan-Laser LP, and the detection polarization is varied using a half waveplate (HWP) and a Glan-Thompson LP. The variation of the detection polarization is realized by rotating the HWP.

2.3 Time domain optics: time-resolved Kerr rotation spectroscopy

Since the invention in 1970, time-resolved Kerr rotation (TRKR) and Faraday rotation (TRFR) spectroscopy have been proven powerful techniques in spintronics research. The direct measurement of the spin dynamics in the time domain allows for the observation of spin coherent transport[26], electric spin injection[27], spin relaxation and dephasing[21,28], and spin Hall effect[29,30]

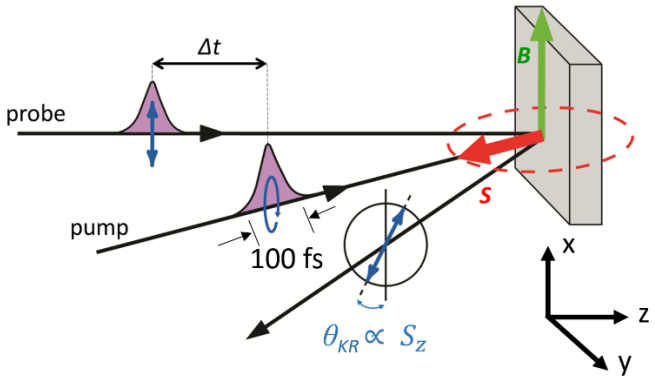

Fig 2.4 Schematic diagram illustrating the principle of operation of the time-resolved Kerr rotation spectroscopy. A circularly-polarized pump pulse creates a spin polarization *S* (red arrow) which Larmor precesses along the applied transverse magnetic field *B* (green arrow). A time-delayed probe pulse measures the *z*-component of the spin precession via the Kerr effect, manifesting by a Kerr rotation of the polarization direction. The time delay between the pump and probe pulse *Δt* is systematically varied in order to map out the time evolution of the spin precession.

The difference between the TRKR and TRFR lies in the measurement geometry. TRKR is performed in reflection geometry while TRFR is a transmission measurement. The principle of operation of TRKR is illustrated in Fig. 2.5. First, a circularly polarized laser pulse is employed to create a transient spin polarization in the sample via optical

selection rules. This is the optical orientation process described in Section 1.2.5 and 2.1 and more details can be found there. In the presence of a transverse magnetic field, the electron spin ensemble that initially orients along the propagation direction of the pump pulse starts to precess along the magnetic field, known as the Larmor precession. A time-delayed linear polarized probe pulse then measures the projection of this ensemble spin vector onto the light propagation direction via the optical Kerr effect, resulting in a Kerr rotation of the linear polarization of the probe pulse. The underlying mechanism for the Kerr effect is the state-filling induced change in the absorption coefficient and index of reflection. As the circularly polarized pump pulse introduces spin-oriented carriers into the conduction band (Fig. 1.3 (a)), the optical absorption in the pump helicity channel is reduced as a result of the state filling, leading to a shift in the absorption and the index of reflection (Fig. 2.5). For the linear polarized probe, the shift in the index of reflection gives rise to the circular birefringence, resulting in a rotation of its linear polarization. Kerr effect is most pronounced in the vicinity of the band edge because the pump-induced state filling predominantly happens near the band edge due to the fast thermal relaxation.

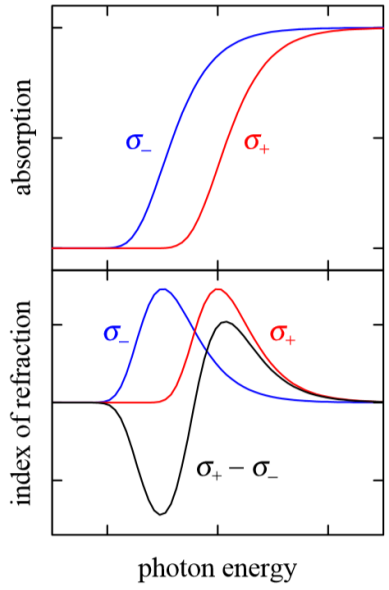

Fig 2.5 State-filling-induced change in the absorption coefficient and index of reflection. Figure adopted from Ref [31].

The time resolution in the TRKR technique is realized by mechanically extending one of the optical path lengths to tune the relative time delay between the pump and probe pulse. The time resolution is ultimately determined by the pulse width of the probe beam, typically on the order of 100 fs. By systematically varying the time delay, the Kerr rotation time trace (θ_{KR} vs. Δt) reveals the temporal evolution of the photo-excited electron spins and can be described by the following equation[32]

$$\theta_{KR}(\Delta t) = \theta_0(e^{-(\Delta t/T_2^*)} + N_0 e^{-(\Delta t/T_h)})\cos(\omega_L \Delta t + \phi) \quad (2.6)$$

where θ_0 is the maximal Kerr angle and N_0 is the ratio of photo-excited to equilibrium carriers at $\Delta t = 0$, T_2^* is the ensemble transverse electron spin dephasing time, T_h is the hole carrier lifetime, $\omega_L = g\mu_B B_{tot}/\hbar$ is the Larmor precession frequency, ϕ is the phase of the

spin precession, and B_{tot} is the total magnetic field experienced by the spins. The two exponential terms reflect the fact that the spin polarization can live much longer than the lifetime of the photo-excited carriers, with the former extending up to nanoseconds and the latter typically less than 100 ps[33]. Independent of lifetime effects, ω_L provides a local magnetometry that measures both the applied field, B_{app}, and any local effective fields, B_{loc}, experienced by the photo-excited electron spins, $B_{tot} = B_{app} + B_{loc}$.

The experimental implementation of the TRKR technique is shown in Fig. 2.6. A degenerate pump-probe setup is employed. An optical pulse of 100 fs and repetition rate of 76 MHz duration was generated by a mode-locked Ti:sapphire laser. A beam-splitter (BS) separates the output of the laser into a pump and probe beam with the intensity ratio of 7:1. The polarization of the excitation is prepared using a Glan-Laser linear polarizer and a calibrated photoelastic modulator (PEM) that allows for a polarization modulation between σ^+ and σ^- polarization at 42 kHz. The probe beam is linearly polarized, prepared by a Glan-Laser linear polarizer. An optical chopper is placed in the probe beam path, providing an intensity modulation at ~500 Hz. The time delay between the pump and probe pulse is realized by a mechanical delay line which reduces the optical path length of the pump beam. The delay line is modified as described in Ref [34] for achieving diffraction-limited autoalignment. The Kerr rotation is measured using a balanced photodiode bridge and lock-in detection. Rotation angles on the order of 1 microradian can be detected.

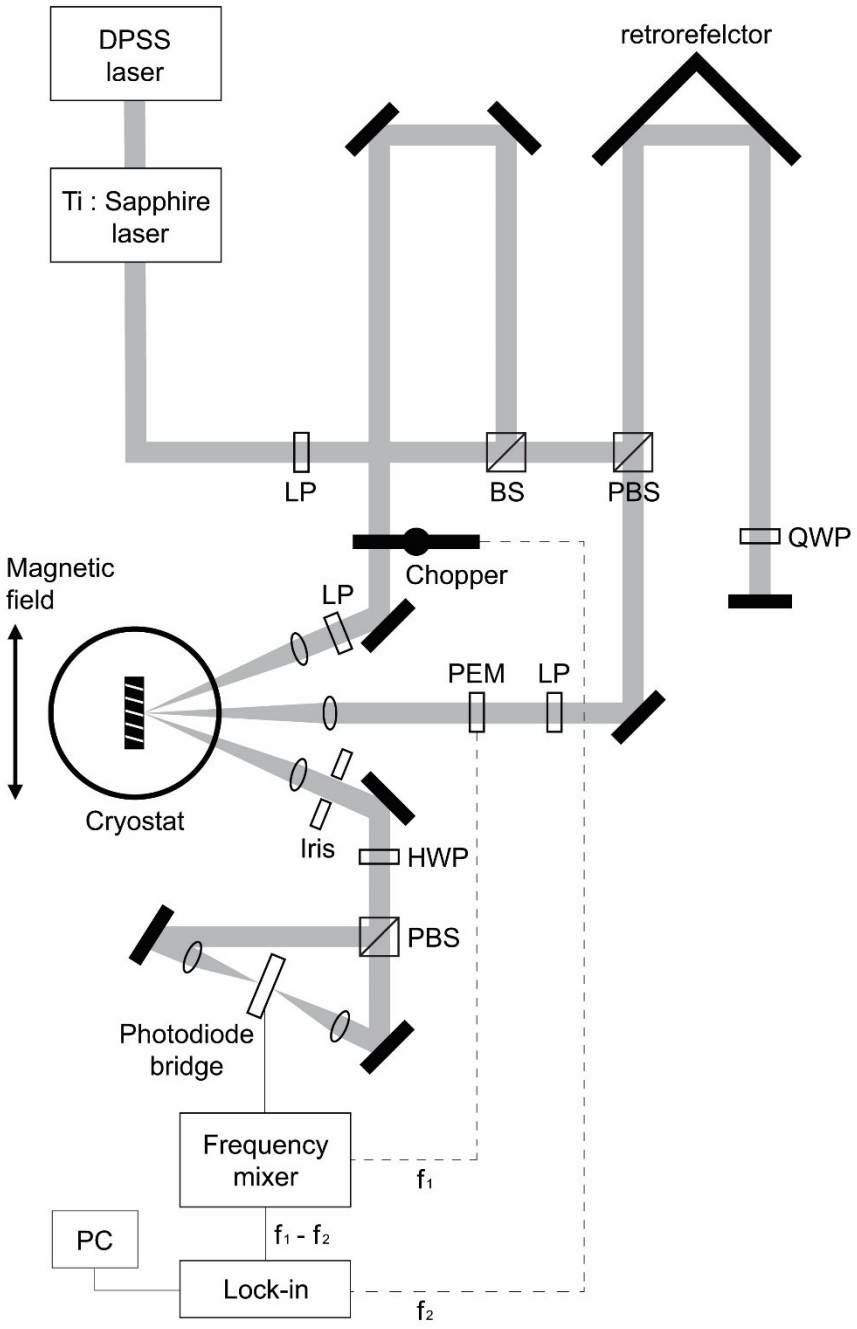

Fig 2.6 Schematic of the time-resolved Kerr rotation setup.

Chapter 3: Exchange-driven spin relaxation in ferromagnetic/oxide/semiconductor heterostructure

3.1 Introduction

Gallium arsenide has a long history as a canonical test bed for the investigation of fundamental spin relaxation properties[17,21,35] and the development of prototype spintronic structures based on ferromagnet (FM)/GaAs heterostructures[36–38]. For example, it would be natural to use FM/GaAs heterostructures to elucidate the dynamic exchange mechanisms underlying the recent development of novel ferromagnetic resonance (FMR)[39–42] and thermally-driven spin injection processes[43–47]. Together with the ultrafast pump-probe spectroscopies which probe GaAs spin dynamics directly in the time domain[21], it would in principle allow for a direct measurement of the dynamic exchange coupling and dissipation at FM/GaAs interfaces.

However, despite the long history and enormous potential in GaAs based systems, there remain crucial questions regarding the fundamental spin relaxation/dissipation processes in the GaAs spin channel itself. Specifically, spin-phonon coupling[48], energy dependence of the Lande g-tensor[49], and inhomogeneities in the hyperfine interaction[50] have all been proposed to explain the low-temperature (< 50 K) spin relaxation in the presence of an applied magnetic field. This absence of clarity prevents the continued use of GaAs based heterostructures to explore emerging areas of current interest.

Here we present a systematic investigation of the free carrier spin lifetime in Fe/MgO/GaAs heterostructures and bare GaAs films that identifies inhomogeneities in the hyperfine interaction due to the random distribution of Si donors, as proposed in Ref [50], as the limiting mechanism in determining the spin relaxation rate in this critical experimental regime. By examining Fe/MgO/GaAs heterostructures, we are able to access large effective nuclear fields due to the exchange-driven hyperfine coupling at low applied field (< 3kG). Comparable nuclear fields in bare GaAs require applied fields on the order of 10s of kG. This ability to tune the nuclear field using exchange coupling allows us to demonstrate the importance of inhomogeneous nuclear fields in governing electron spin relaxation in both bare GaAs films and FM/GaAs heterostructures. Thus we resolve a long-standing and contentious question of the origin of the spin lifetime in low temperature GaAs when a magnetic field is present. This more complete understanding in turn allows a quantitative description of the dynamic, exchange mediated, electron-nuclear interactions in our FM/GaAs nanostructures.

3.2 Experimental

3.2.1 Sample preparation

The schematic structure of the samples studied in this work is shown in Fig. 3.1 (a), with layer thicknesses of: 8 nm MgO/10 nm Fe/0.2 nm MgO/120 nm Si doped n-GaAs ($7 \times 10^{16}/cm^3$)/400 nm $In_{0.5}Ga_{0.5}P/n^+$-GaAs (100) substrate. These samples were synthesized according to Ref [51] with the following modifications: First, $In_{0.5}Ga_{0.5}P$ is substituted for $Al_{0.7}Ga_{0.3}As$ as the stop etch layer, and is grown with the n-GaAs layer in a commercial metal-organic chemical vapor deposition system (NanoTech West Laboratory at The Ohio State University). Second, to achieve a clean GaAs surface for the deposition of epitaxial Fe/MgO, the samples are transferred in air to a III-V molecular beam epitaxy (MBE) system where the surface oxide on n-GaAs is desorbed in an As atmosphere and an As capping layer is deposited. This capping layer prevents oxidation during a second transfer in air to a separate oxide/metal MBE system for the deposition of the Fe/MgO. The thickness of the MgO layer has been optimized to maximize the exchange coupling at the Fe/GaAs interface[51].

The samples studied in this work is synthesized by Patrick M. Odenthal from the Roland Kawakami group at The University of California Riverside, and John A. Carlin from the Institute for Materials Research at The Ohio State University

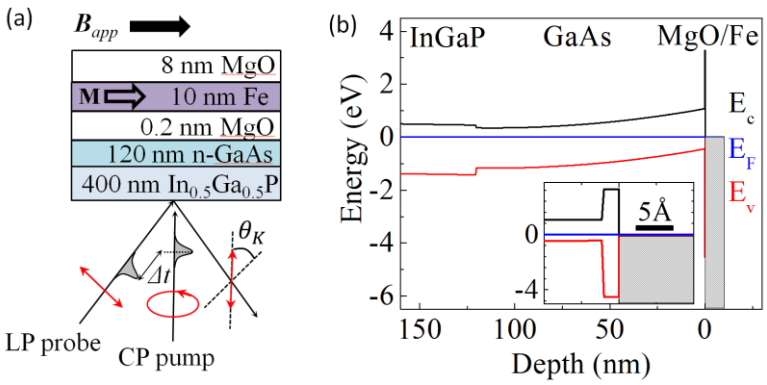

Fig 3.1 (a) Schematic of sample structure and time-resolved Kerr rotation (TRKR) measurement geometry. (b) Simulated band structure for sample in (a). Inset: calculated band structure near the GaAs/MgO/Fe interface showing that the Fermi level is pinned at 0.3 eV above the GaAs valence band maximum.

Fig. 3.1 (b) shows the simulated band structure of the sample calculated using a self-consistent one-dimensional Schrödinger/Poisson solver (BandEng). The band offset at the interface (Fig. 3.1 (b), inset) is determined by previous studies using x-ray and ultraviolet photoelectron spectroscopies to study the band structure of Fe/MgO/GaAs tunnel junction[52].

A control sample is grown with a similar structure but without the Fe/MgO layer, and both samples are mounted face-down on 100 μm thick sapphire wafers so that the n^+-GaAs substrates can be removed by selective wet etching using the $In_{0.5}Ga_{0.5}P$ layer as a chemically-selective etch stop[53].

3.2.2 TRKR spectroscopy

TRKR spectroscopy is performed to probe the spin dynamics. Laser pulses of 130-fs duration and 76 MHz repetition rate are generated by a mode-locked Ti-Sapphire laser, and are split into pump and probe pulse trains whose time delay, Δt, is controlled by a mechanical delay line. The pump/probe power ratio is ~7, and the time-averaged pump power density is 119 W/cm^2. The details of the experimental setup can be found in Section 2.2.

3.3 Ferromagnetic proximity polarization effect

3.3.1 Examination of FPP effect

Since the fabrication of the Fe/MgO/GaAs heterostructure involves ex-situ transfers between growth systems as well as wet chemical etching, we explore the strength of the interfacial exchange interaction via time-resolved Kerr rotation (TRKR) [54,51,55] to evaluate the interface quality. This characterization is motivated by previous reports of the so-called "ferromagnetic proximity (FPP) effect" in MnAs/GaAs[54,55], Fe/GaAs[51,5555] and Fe/MgO/GaAs[51] heterostructures.

The TRKR time scans for both the Fe/MgO/GaAs heterostructure and the GaAs control are shown in Fig. 3.2. Scans are acquired at a temperature T = 5 K and an applied field $\boldsymbol{B_{app}}$ = 12 kG. A clear difference in ω_L (or equivalently, B_{tot}) between the Fe/MgO/GaAs and GaAs structures implies a variance in B_{loc} between the two samples (roughly -2 kG and +0.2 kG, respectively). The magnitude and sign of B_{loc} in Fe/MgO/GaAs is consistent with previous FPP measurements, and has been attributed to a hyperpolarization of the Ga and As nuclei[22,55].

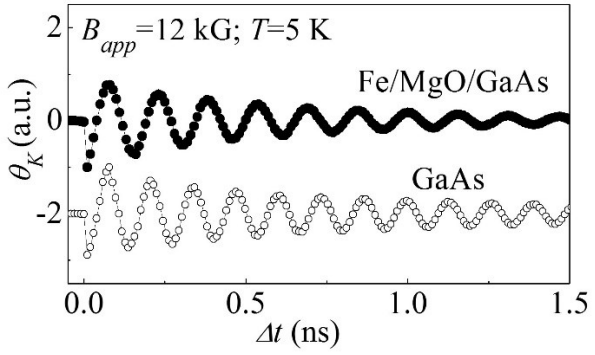

Fig 3.2 Measured Kerr rotation (θ_K) vs Δt for a Fe/MgO/GaAs heterostructure (solid circles) and a control GaAs epilayer (open circles) at T= 5 K and $\boldsymbol{B_{app}}$= 12 kG. The data are offset for clarity.

Fig. 3.3 shows a schematic diagram detailing the fundamental interactions underlying this effect. In the presence of a transverse $\boldsymbol{B_{app}}$, a non-equilibrium electron spin population with a net polarization $\boldsymbol{S_0}$, is excited in the GaAs layer by the circularly polarized optical excitation. From this initial population, we consider separately free carrier spins that reflect from the Fe/MgO layer[56] and spins that evolve purely within the GaAs. The former will acquire a net orientation parallel to the magnetization of the Fe layer through the FPP effect, $\boldsymbol{S_{FPP}}$, while the latter will relax antiparallel to the applied field, $\boldsymbol{S_{rel}}$, through the Zeeman relaxation process The opposite orientation of $\boldsymbol{S_{rel}}$ with respect to the applied field is a result of a negative Lande g-factor in GaAs, which is -0.44[57]). These two non-equilibrium electron spin populations both act to dynamically polarize nuclear spins ($\boldsymbol{I}$) via the hyperfine interaction ($H_{hyperfine}= A\boldsymbol{I}\cdot\boldsymbol{S_i}$, where A is the product of nuclear and electron Bohr magneton and the probability density of electron wave function at the nuclear sites and i = *rel* or *FPP*), a process known as dynamical nuclear polarization (DNP. For more information, look at section xxx). For $\boldsymbol{B_{app}}$ much larger than the nuclear dipole-dipole field (~10G) and Knight field (~100G), the polarized nuclear spins in turn create an effective local field $\boldsymbol{B_n^{tot}}$ acting on the photo-excited spin[17,58] .

$$\boldsymbol{B_n^{tot}} \propto -\boldsymbol{B_{app}}\left(\boldsymbol{B_{app}}\cdot\left(\boldsymbol{S_{rel}}+\boldsymbol{S_{FPP}}\right)\right)/{B_{app}}^2 \tag{3.1}$$

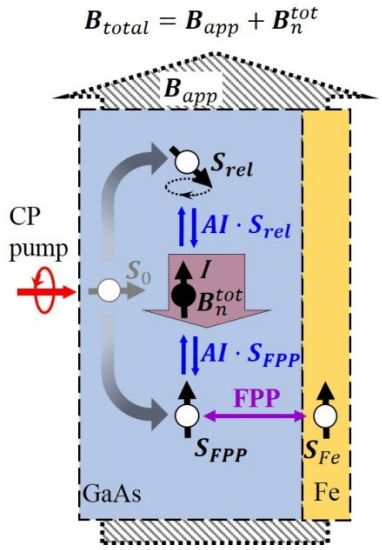

Fig 3.3 A cartoon illustrates that a nuclear field antiparallel to the applied field in a Fe/MgO/GaAs heterostructure results from the hyperfine coupling between GaAs nuclear spins (***I***), and two non-equilibrium spin populations, $\boldsymbol{S_{rel}}$ and $\boldsymbol{S_{FPP}}$.

Since $\boldsymbol{S_{FPP}}$ is antiparallel to $\boldsymbol{S_{rel}}$, the resulting $\boldsymbol{B_n^{tot}}$ can be antiparallel (negative sign) or parallel (positive sign) to $\boldsymbol{B_{app}}$, depending on the competition between the FPP and Zeeman relaxation mechanisms. The observation of B_n^{tot} = -2 kG in Fe/MgO/GaAs (Fig. 3.2) indicates that $\boldsymbol{B_n^{tot}}$ is dominated by $\boldsymbol{S_{FPP}}$ while in the GaAs control B_n^{tot} is positive (= +0.2 kG), as expected from the nuclear polarization arises from $\boldsymbol{S_{rel}}$.

This analysis identifies the local magnetic field identified by the Larmor magnetometry shown in Fig. 3.2, B_{loc}, as arising from an effective nuclear field, B_n^{tot}, due to the optically induced non-equilibrium nuclear polarization. Further evidence for the nuclear origin of B_{loc} can be found in the resonant suppression of B_{loc} at the various nuclear magnetic resonance (NMR) frequencies of the Ga and As nuclei (See Section 3.3.2).

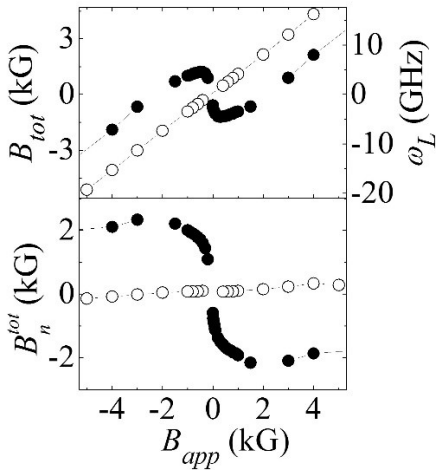

Fig 3.4 Top panel: total field $\boldsymbol{B_{tot}}$ (Larmor frequency ω_L) extracted from TRKR time trace as a function of $\boldsymbol{B_{app}}$ for Fe/MgO/GaAs (solid circles) and bare GaAs (open circles) at T= 5 K. Bottom panel: nuclear field $\boldsymbol{B_n^{tot}}$ ($\boldsymbol{B_n^{tot}} = \boldsymbol{B_{tot}} - \boldsymbol{B_{app}}$) as a function of $\boldsymbol{B_{app}}$.

Although the magnitude and sign of $\boldsymbol{B_n^{tot}}$ in Fe/MgO/GaAs is a strong indication of FPP, more compelling evidence is the ferromagnetic imprinting of the nuclear spin polarization[54,55]. As can be seen in Fig. 3.4, the dependence of $\boldsymbol{B_{tot}}$ on $\boldsymbol{B_{app}}$ (top panel) has both a linear component (from the Larmor dependence on $\boldsymbol{B_{app}}$) and a component that tracks with the magnetization of the Fe layer, switching at fields below the experimental resolution (~ 0.02 kG) and saturating at $\boldsymbol{B_{app}}$ ~ ±3 kG. This behavior is more clearly seen in the bottom panel of Fig. 3.4 where the linear field dependence has been subtracted. This is in contrast to the behavior in the GaAs control, where $\boldsymbol{B_{tot}}$ (ω_L) and $\boldsymbol{B_n^{tot}}$ scale linearly with $\boldsymbol{B_{app}}$ (open circles)[17,58,59]. These results are both quantitatively and qualitatively consistent with previous studies[54,55], and confirm the high interfacial quality of the sample despite the multiple ex-situ transfers and wet etching involved in the growth and fabrication process.

3.3.2 Confirmation of nuclear fields

The premise that the difference between the local field measured by the Larmor precession of the electrons in Fig. 3.2 and the applied field is due to hyperfine coupling is supported by the existing FPP literature and the lab-time dependence of the TRKR signal (the signal evolves on the scale of minutes when the experimental parameters are changed). This hypothesis can be further validated by exploring the resonant depolarization of the presumed nuclear spin orientation using the repetition rate of the pulsed laser (76 MHz) as a periodic tipping pulse[60,61,62]. This depolarization can be driven by two processes: (1) the electron spins excited by periodic laser pump pulses generate an effective periodic hyperfine field that resonantly depolarizes a specific nuclear species at appropriate applied field; (2) periodically photo-excited carriers create a modulated electric field that in turn induces quadrupolar resonance of a specific nuclear species. The quadrupolar resonance in case (2) occurs at half of the applied field in case (1) because it involves a transition of $\Delta m = 2$ (m is nuclear spin quantum number) rather than a $\Delta m = 1$ transition, as in (1).

A sensitive and less time-consuming approach for probing this optically-pumped NMR can be accomplished by measuring the Kerr rotation angle (θ_K) as a function of applied field ($\boldsymbol{B}_{app}$) at fixed delay time (Δt). As can be seen in Eq. (1) in the main text θ_K has the same functional dependence on $\boldsymbol{B}_{tot}$ and Δt, so in the absence of nuclear effects (when $\boldsymbol{B}_{tot} = \boldsymbol{B}_{app}$) varying $\boldsymbol{B}_{app}$ should have the same effect as varying Δt, i.e. an oscillating cosine with frequency given by $g\mu_B\Delta t/\hbar$. When nuclear effects are included, the additional hyperfine field, $\boldsymbol{B}_n$, results in a phase shift of these oscillations off-resonance that is

abruptly suppressed with $\boldsymbol{B_{app}}$ matches the resonance condition for one of the nuclear spin species.

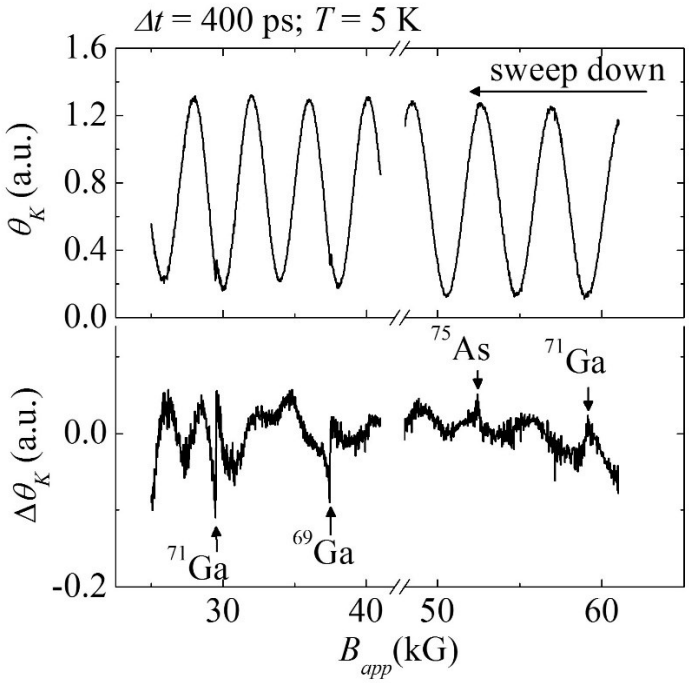

Fig 3.5 All-optical NMR study on Fe/MgO/GaAs heterostructure. Top panel: θ_K as a function of $\boldsymbol{B_{app}}$ at Δt= 400 ps and T = 5 K. Bottom panel: The same data set as the top panel, but the oscillatory background is subtracted for resolving small NMR features

The top panel of Fig. 3.5 shows θ_K as a function of $\boldsymbol{B_{app}}$ at Δt = 400 ps and T = 5 K. To clearly resolve the NMR features, the oscillatory background is subtracted, as shown in the bottom panel. Four resonance peaks at $\boldsymbol{B_{app}}$= 59.1 kG, 52.4 kG, 37.5 kG and 29.5 kG correspond to nuclear dipole resonance of ^{71}Ga (γ = 1.02475 MHz/kG), and nuclear quadrupolar resonances of ^{75}As (γ = 0.73148 MHz/kG), ^{69}Ga (γ = 1.30204 MHz/kG) and ^{71}Ga respectively. These results are consistent with previous all-optical NMR studies on

bulk GaAs[60] and GaAs quantum wells[61,62], and confirm the nuclear origin of the local field in Fe/MgO/GaAs heterostructures.

3.4 Exchange-driven spin relaxation

3.4.1 Impact of interfacial exchange coupling

We now consider the impact of this interfacial exchange coupling and consequent nuclear polarization on the spin relaxation/dissipation in the GaAs layer. Fig. 3.6 (a) and (b) show T_2^* and the magnitude of $\boldsymbol{B_n^{tot}}$ ($|\boldsymbol{B_n^{tot}}|$) as a function of applied field, $\boldsymbol{B_{app}}$, respectively. A remarkable correlation is evident, with $|\boldsymbol{B_n^{tot}}| \sim 1/T_2^*$. There are two distinct regimes evident in these measurements. First, for $|\boldsymbol{B_{app}}|$) below 0.5 kG, there is a strong enhancement of T_2^* and concurrent suppression of $|\boldsymbol{B_n^{tot}}|$. This is a well-known effect arising from the nuclear depolarization driven by the nuclear dipole-dipole coupling[17,58]. Second, for fields above 0.5 kG there is a competition between the nuclear field generated by the FPP effect, $\boldsymbol{B_n^{FPP}}$, and the nuclear field generated by conventional spin relaxation from Zeeman splitting in the conduction band, $\boldsymbol{B_n^{Z}}$. As can be seen in Fig. 3.4, with increasing $\boldsymbol{B_{app}}$ the FPP driven polarization is initially much larger than the Zeeman driven polarization, but saturates as the magnetization saturates at $B_{app} \sim 3$ kG. In contrast, the Zeeman driven polarization grows slowly but continuously, increasing linearly for the entire field range studied here. Since these two contributions have opposite sign (Fig. 3.3 and Fig. 3.4) their competition gives rise to an inflection point in the total nuclear field, $\boldsymbol{B_n^{tot}} = \boldsymbol{B_n^{FPP}} + \boldsymbol{B_n^{Z}}$, as can be seen in the maximum in $|\boldsymbol{B_n^{tot}}|$ in Fig. 3.6 (b).

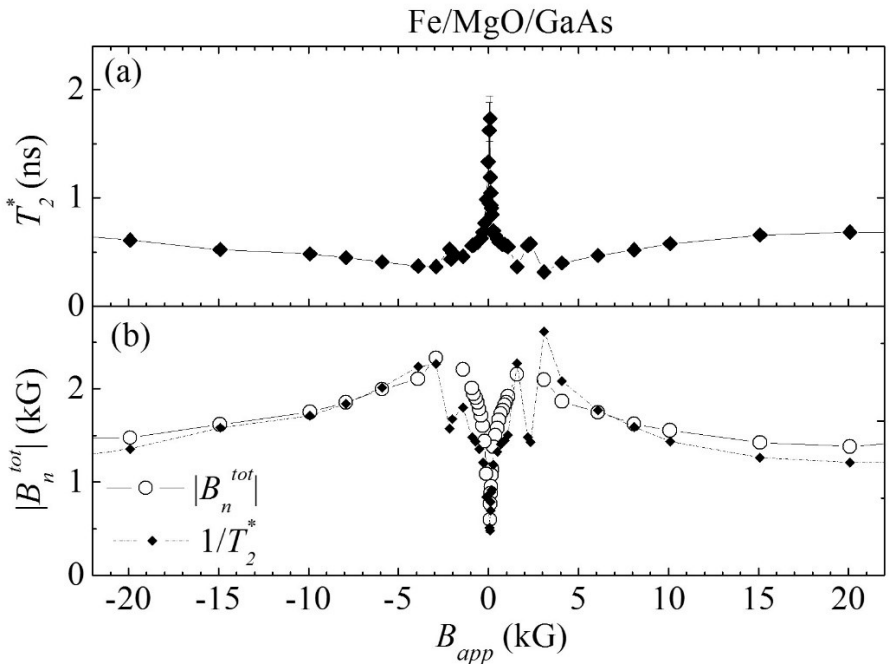

Fig 3.6 (a) Spin relaxation time (T_2^*, solid diamonds) and (b) $|B_n^{tot}|$ (open circles) and $1/T_2^*$ (solid diamonds) as a function of B_{app} for Fe/MgO/GaAs up to 20 kG at T= 5 K.

3.4.2 Inhomogeneous nuclear model and experimental validation

In general, this correspondence between $|\boldsymbol{B_n^{tot}}|$ and T_2^* strongly indicates that the dominant spin relaxation in this regime is via hyperfine coupling. To gain insight into the origin of this hyperfine-dominated spin relaxation, we consider a theory in which the inhomogeneous nuclear field is due to the non-uniform donor distribution in the GaAs (Fig. 3.7), leading to inhomogeneous dephasing of the photo-excited electron spins[50]. In this theory, $\boldsymbol{S_{FPP}}$ and $\boldsymbol{S_{rel}}$ can both relax into donor-bound localized states surrounding the Si dopants in the GaAs as shown in the left panel of Fig. 3.7. These trapped spins can either directly hyperpolarize nuclei within their Bohr radius (path 1) or polarize donor electrons via the exchange interaction[17,63] that then hyperpolarize surrounding nuclei (path 2),

resulting in a puddle of hyperpolarized nuclear spin oriented either parallel (FPP) or anti-parallel (Zeeman) to $\boldsymbol{B_{app}}$. These randomly located polarized nuclei in turn give rise to an inhomogeneous nuclear field distribution that leads to the dephasing of itinerant photo-excited carriers that move across those donor sites.

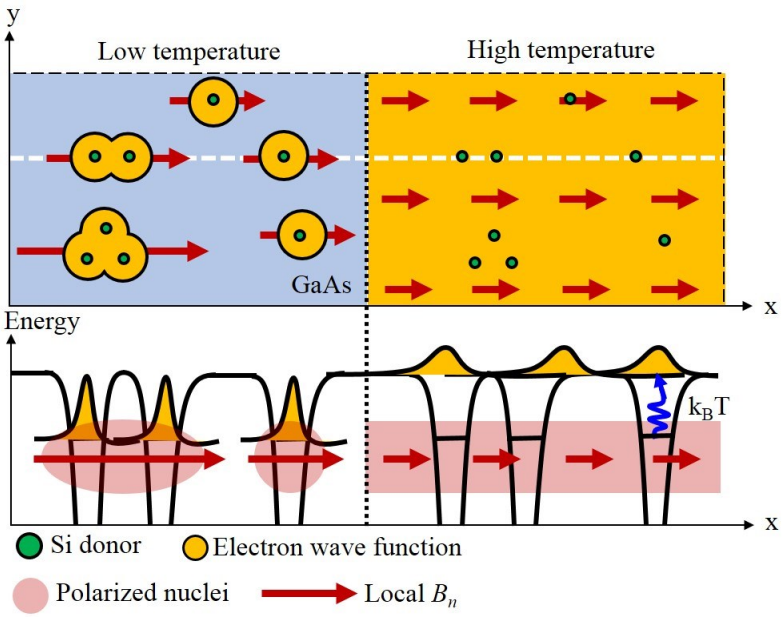

Fig 3.7 Schematics of nuclear field distribution due to the random silicon donor distribution (top panels) and the carrier trapping potential (bottom panels) at low temperature (left panels) and high temperature (right panels). At low temperature, the random spatial distribution of silicon donors (top left panel) leads to an inhomogeneous nuclear field as electron spins get trapped at the donor sites and hyperpolarize the surrounding nuclei (bottom left panel). At high temperature, a homogeneous nuclear field distribution is obtained (top right panel) due to the delocalization of trapped carriers (bottom right panel).

The spin relaxation via path 1 can be calculated using a theory of continuous-time-random-walk for spin[64,65]. As was recently shown in Ref [50], in the motional narrowing

limit the existence of the nuclear field inhomogeneity gives rise to an anisotropic spin relaxation term, $1/T_2^* \sim (B_n^{tot})^2$, which fits our data at T= 5K well, supporting the validity of this interpretation (data not shown here).

Critically, this theory makes two implicit predictions about the expected behavior of T_2^* as a function of the temperature of the sample, T, and $\boldsymbol{B_{app}}$. Considering first the effect of the sample temperature, we note that raising the system temperature should weaken the hyperfine coupling due to the thermal activation of localized carriers[17]. This in turn should lead to a more homogeneous nuclear field as well as an overall decrease in $|\boldsymbol{B_n^{tot}}|$ as thermal depolarization of the nuclear bath competes with dynamic nuclear polarization as shown in the right panel of Fig. 3.7. This decrease in inhomogeneity in the nuclear field should in principle lead to an enhancement of T_2^*.

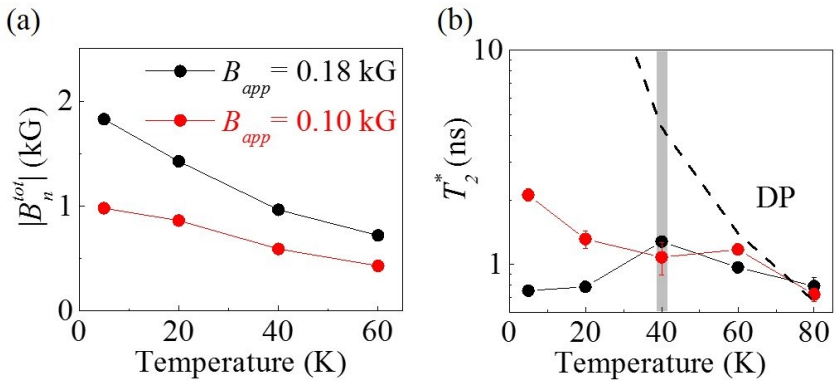

Fig 3.8 (a) $|\boldsymbol{B_n^{tot}}|$ and (b) T_2^* as a function of temperature for $\boldsymbol{B_{app}}$= 0.18 kG (black circles) and 0.10 kG (red circles). The black dashed line is the DP prediction of the temperature dependence of T_2^*.

These trends are clearly observed in the temperature dependent data presented in Fig. 3 (a) and (b) for $|\boldsymbol{B_n^{tot}}|$ and T_2^*, respectively. Considering first data taken for $\boldsymbol{B_{app}}$ =

0.18 kG (black circles) and at temperatures below 40 K, we see a monotonic decrease in $|\boldsymbol{B_n^{tot}}|$ and a monotonic increase in T_2^* for increasing temperature. For temperatures above 40 K, the trend in $|\boldsymbol{B_n^{tot}}|$ continues to monotonically decrease but the increase in T_2^* shows a local maximum, with T_2^* decreasing for higher temperatures. This behavior is qualitatively consistent with a continuous decrease in the strength of hyperfine-induced dephasing of the spin ensemble until it is no longer the dominant spin relaxation mechanism and is quantitatively consistent with the temperature scale for the thermal ionization of the Si dopants (full ionization is expected at roughly 69 K[66]. Comparison of the high temperature behavior of T_2^* with previous reports in bare GaAs[21] suggests that this regime is dominated by D'yaknov-Perel (DP) spin relaxation[21,48] (dashed black line).

We note that this non-monotonic temperature dependence of T_2^* was also observed in bare GaAs, but at much higher $\boldsymbol{B_{app}}$ (> 10 kG)[21,67], and is inconsistent with the recent prediction that spin-phonon coupling is the dominant spin relaxation pathway at low temperature in the presence of a significant $\boldsymbol{B_{app}}$[48]. The derived spin relaxation rate based on the spin-phonon coupling model is proportional to $(B_{app})^2$ at a fixed temperature, and in the low $\boldsymbol{B_{app}}$ region discussed here, the rate is too small to account for the measured magnitude of T_2^*. A comparison with previous studies[21,60,67] suggests that our theory of spin relaxation via inhomogeneous nuclear fields may also be applied to bare GaAs when a large nuclear field (~1 kG) is present. This can be achieved by optically pumping a non-equilibrium nuclear polarization at large $\boldsymbol{B_{app}}$ (>10 kG)) in our measurement geometry. Our results, both in Fe/MgO/GaAs and bare GaAs samples, clearly identify the peak of T_2^* as

the outcome of competition between two spin relaxation mechanisms, inhomogeneous hyperfine interactions and DP spin relaxation.

The second, correlated, prediction of our model is that suppressing the hyperfine coupling should cause the local maximum in T_2^* at 40 K to disappear and allow the next most dominant spin relaxation mechanism (presumably DP in these samples) to be evident at all temperatures. The low data in Fig. 3.6 provide a path to realizing just such a measurement through the low field dipole-induced depolarization of $|\boldsymbol{B_n^{tot}}|$. Reducing $\boldsymbol{B_{app}}$ from 0.18 kG to 0.10 kG dramatically reduces $|\boldsymbol{B_n^{tot}}|$ from +2 kG to +1 kG at T= 5 K, and the data in Fig. 3.8 (a) show that this suppression persists to higher temperature. This reduction in nuclear spin polarization leads to a suppression of the local maximum in T_2^* at 40 K, and T_2^* converges toward the DP prediction across the entire measured temperature range, as predicted above. The failure to fully recover the DP prediction can be explained by the fact that the finite length of our mechanical delay line and laser repetition rate place a lower bound on the value of $\boldsymbol{B_{app}}$ for which we can experimentally resolve T_2^*. As a result, we cannot fully suppress $|\boldsymbol{B_n^{tot}}|$ and therefore must measure in a regime with some residual hyperfine-driven inhomogeneity.

3.5 Summary and outlook

In conclusion, we observe a strong dependence of electron spin relaxation time on the FPP-enhanced hyperfine field in Fe/MgO/GaAs heterostructures. Our results are consistent with a model of inhomogeneous broadening of the effective nuclear field due to carrier localization at Si donors at low temperature, and clarify the origin of a local maximum in the value of T_2^* as a function of temperature. This work establishes a comprehensive fundamental framework for understanding spin relaxation/dissipation in GaAs-based FM/normal material (NM) heterostructures that may serve as the basis for coherent, time-resolved studies of spin transfer and dynamic exchange coupling in the emerging field of dynamically driven spin pumping. For example, while the current study focuses on the impact of the FPP process on the GaAs layer, symmetry argues that the exchange driven polarization of the photo-carriers in GaAs must be accompanied by a concurrent *depolarization* of the Fe layer. This opens the door to future studies exploring the nature of this spin transfer, including its dependence on resonant (microwave) and thermal excitation of the magnetization of the ferromagnetic layer.

Chapter 4:

Toward all-optical approaches to probing spin dynamics in quasi-one-dimensional semiconductors

4.1 Introduction

Since the discovery of the long spin relaxation time of itinerant electrons up to 100 nanoseconds and spin diffusion length over 100 μm in GaAs, extraordinary advances in semiconductor spintronics have been made in the past one and half decade[21,26,32]. Most of the efforts in this field were devoted to two-dimensional (2D) systems such as quantum wells (QW). Spin relaxation and spin injection/detection have been characterized in 2D III-V and II-VI semiconductors as well as in Si using optical pump-probe techniques and spin-polarized electroluminescence (EL)[36,37,29,68–76]. In addition, spin relaxation in bulk semiconductor and semiconductor quantum dots (QD), which are 3D and 0D systems, respectively, has also been well studied, revealing intriguing spin physics.

What is clearly missing is the investigation of spin dynamics and spin transport in 1D semiconductors. The decreased mean free path and momentum focusing found in 1D systems have been predicted to lead to dramatic increases in spin relaxation time[5–7,77] and observed experimentally in InGaAs QW channels with widths between 20 μm and 420 nm[78]. In addition, if spin-based electronics is to compete as a next-generation electronics

technology, it is essential to understand spin physics in 1D semiconductors since future spintronic devices will most likely function with feature size of tens of nanometers.

Despite progress on transport-based approaches, optical probes that are matured and commonly employed in 3D (bulk), 2D (quantum wells) , or 0D (quantum dots) semiconductor materials have been rendered ineffective in 1D systems as a result of optical polarization anisotropy inherent in 1D. The geometric confinement results in optical absorption and emission preferentially occur in the direction parallel to the axis of the 1D system, and less-favored in the perpendicular direction. The degree of optical polarization anisotropy is determined by the dielectric contrast between the 1D system and its environment. For most semiconductors, the dielectric constant is large (usually around 10. e.g. $\varepsilon_{GaAs} \sim 10.89$) relative to that of the environment (e.g. $\varepsilon_{air} \cong 1$), leading to a preferential absorption and emission for light that is linearly polarized along the nanowire axis. Consequently, this dielectric-induced polarization anisotropy prohibits optical spin excitation by circularly polarized light and optical spin detection through luminescence of circularly polarized light or Kerr rotation of a linear polarized light.

As a first attempt to tackle this fundamental challenge and move towards investigation of spin dynamics in 1D, we propose a dielectric-matched method basing on GaAs/AlGaAs core-shell nanowires. Metalorganic chemical vapor deposition (MOCVD), a proven technique in producing a variety of 1D and 0D heterostrctures in semiconductor nanowires, is employed to implement this design. With well controlled geometry and excellent crystal quality[79–81], MOCVD readily produces a core-shell structure wherein the shell ($Al_xGa_{1-x}As$) of sufficient thickness provides superb dielectric matching to the core

nanowire (GaAs) (ε_{GaAs}:ε_{AlGaAs}= 10.89:10.07). Additionally, the core-shell nanowire structure offers passivation of the surface of the core GaAs wire and greatly enhances optical efficiency. Both aspects are crucial in optical spin excitation and detection experiments.

In the following sections, major efforts on moving toward the ultimate goal of optical investigation of spin dynamics in 1D are present. They include:

1. Synthesize GaAs/AlGaAs core-shell nanowires using MOCVD with special focus on the impact of growth aspects (core growth temperature and substrate orientation) on the optical characteristics. (Section 4.2)
2. Suppress optical polarization anisotropy in GaAs/AlGaAs core-shell nanowires by dielectric matching. In parallel, similar control of polarization anisotropy is realized in ZnO/Ta_2O_5 cores-shell nanowires, demonstrating the universal validity of this approach. (Section 4.3)
3. Develop a sample geometry basing on GaAs/AlGaAs core-shell nanowires that address the optical polarization anisotropy and other technical challenges and perform the spin lifetime measurement using pump-probe time-resolved Kerr Rotation (TRKR) technique. (Section 4.4)

4.2 Photoluminescence evolution of GaAs/AlGaAs core-shell nanowires: effects of growth temperature and substrate orientation

Metal-organic chemical-vapor deposition (MOCVD) is a proven technique for semiconductor nanowire growth via the vapor-liquid-solid (VLS) mechanism which has been used to grow III-V nanowire heterostructures for electronic[82] and optoelectronic applications[83]. As with all semiconductor nanostructures, fabrication of high quality materials is the first step toward realizing the full potential of these structures. In particular, for III-V nanowires with high surface-to-volume ratio, minimizing surface defect states is essential[84]. To develop high quality nanowires for the aforementioned optical spin studies, it is necessary to explore how various growth parameters affect the optical properties of the nanowires. Here we report a systematic study of PL evolution of Au-catalyzed GaAs/AlGaAs core/shell nanowires grown on both GaAs (100) and (111)B substrates at varying growth temperatures. Growth temperatures are calibrated *in-situ* to avoid possible drift in the chamber condition, allowing for a systematic and high resolution variation of the growth temperature. The optical quality is quantified by measuring the PL intensity ratio between band-edge and defect-mediated photoluminescence. It is found that defect incorporation as a function of the growth temperature is dependent on the substrate orientation, despite the fact that the direction of the nanowire growth is the same for both substrates (along <111>). Finally, a window in core growth temperature where defects that degrade optical quality may be minimized is identified.

4.2.1 Nanowire synthesis

"Button-up" catalytic growth offers a unique route for synthesis of semiconductor nanowires. In particular, metalorganic chemical vapor deposition (MOCVD) has proved an excellent technique to produce a variety of 1D and 0D heterostructures in semiconductor nanowires with well controlled geometry and excellent crystal quality[79–81]. This capability provides the materials basis for studying spin physics in low dimensional semiconductors. In addition, MOCVD is ideally suited for synthesis of III-V core-shell heterostructures wherein the shell (e.g. $Al_xGa_{1-x}As$) of sufficient thickness provides dielectric matching to the core nanowire (e.g. GaAs). Additional benefits of the core-shell nanowire structure are passivation of the surface of the core wire and greatly enhanced optical efficiency.

In this section, we explore growth aspects, specifically, core growth temperature and substrate orientation, and their impact on the nanowire optical characteristics using photoluminescence spectroscopy (PL).

To prepare substrates for growth, GaAs (100) and (111)B wafers are cut into pieces and placed in an ultraviolet (UV) ozone cleaner to remove any organics absorbed on the surface, this also produces a hydrophilic surface desired for subsequent dispersion of Au nanoparticles. The surfaces are then functionalized with 0.1% Poly-L-Lysine solution (Ted Pella Inc.), rinsed with deionized water (resistivity > 18 MΩ), and dried with N_2. Next, tannic acid capped 40-nm Au colloid suspension (Ted Pella Inc., 7.72×10^{10} particles/mL) is dropped on the surface and allowed to sit for 15 minutes. Excess suspension is removed by blowing the surface dry with a N_2 gun. The substrates with Au nanoparticles are then

placed in an Aixtron 3×2" Close Coupled Showerhead (CCS) MOCVD reactor for nanowire growth.

As reported in the literature,[85–93] III-V nanowire growth requires a balance between the pyrolysis of the organometallic precursors, the solubility of the group III and group V atoms in the Au colloid, and the diffusion of atomic species on the substrate and nanowire surface. As a result, particular care for accurate and reproducible measurements of the substrate temperature during growth is essential. Although pyrometers have been widely used for in-situ measurement of the actual substrate temperature, it is challenging to use pyrometers to monitor GaAs nanowire growth because the typical temperature window for VLS growth of GaAs nanowires is below the range of pyrometers available for MOCVD systems. In our MOCVD reactor, the surface temperature is directly observed in real time with an emissivity-corrected pyrometer that has a lower temperature limit of 480°C while the temperature range for nanowire growth spans from 400°C to 470°C (indicated by the hatched region in Fig. 1). This limitation requires a calibration of the actual substrate temperature above 480°C based on a linear relationship between the pyrometer and thermocouple (TC) readings and a linear extrapolation to lower temperatures. The overall linearity of the temperature response of the system is confirmed by using a pyrometer to measure the temperature of the bare susceptor (triangles in Fig. 1). The estimated error for a given surface temperature generated by this extrapolation is around ±1°C. Substrate temperatures of nominally identical growth conditions are reproducible to within ±3°C.

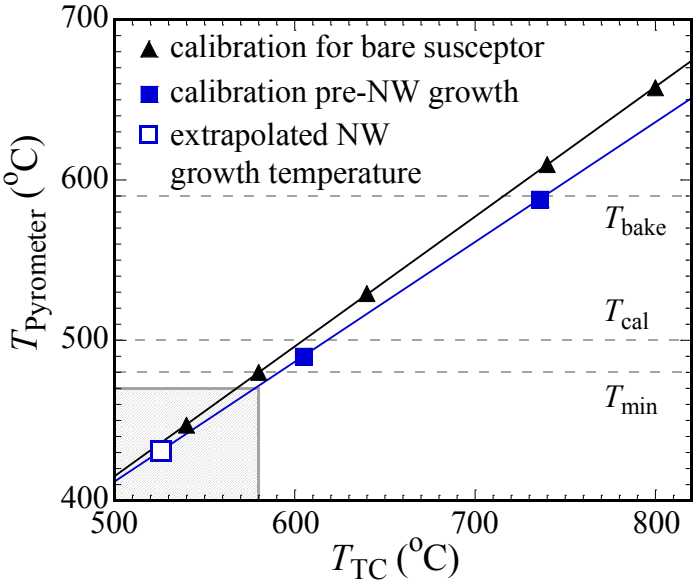

Fig 4.1 Temperature readings of the thermocouple (TC) in the MOCVD susceptor calibrated by a pyrometer on a bare susceptor (triangles) and a susceptor loaded with GaAs wafers before nanowire growth (squares). The pyrometer has a minimum operational temperature of T_{min} = 480°C. The hatched box represents the nanowire growth temperatures (below T_{min}). The actual surface temperatures of GaAs wafers for NW growth are obtained from linear extrapolation.

To desorb surface oxides before nanowire growth, the prepared substrates are baked at 590°C (all temperatures given are actual substrate temperatures) for 15 minutes under an arsine flow of 1040 μmol/min at a pressure of 150 mbar that is maintained for the entire growth. The temperature is then lowered to 500°C and stabilized to monitor the system temperature and extrapolate a growth temperature as shown in Fig. 4.1. Next, the temperature is lowered to the growth temperature between 410 and 472°C and allowed to stabilize. The arsine flow is adjusted to 223.2 μmol/minute and a trimethylgallium (TMGa) flow of 8.6 μmol/minute is introduced into the reactor to begin the GaAs core nanowire

growth. After 15 minutes of nanowire growth, the substrate is heated to 650°C under arsine and a shell of $Al_{0.35}Ga_{0.65}As$ is deposited on the core GaAs nanowires for 3 minutes. For the shell deposition, the TMGa and AsH_3 flows are adjusted to 26 μmol/minute and 1786 μmol/minute respectively, with an additional flow of trimethyaluminum (TMAl) at 10.3 μmol/minute. These AlGaAs shell growth conditions are identical across the entire sample set. The quoted Al composition is nominal and is based on the characterization of previous thin film growths using the same reactor conditions. The role of the $Al_{0.35}Ga_{0.65}As$ shell is to passivate the surface of the GaAs core, protecting it from the formation of surface defect states.[84,94] While there may be a deviation from the targeted 35% Al, the Al composition should be consistent for all samples.

The samples studied in this work is synthesized by Nicholas Minutillo from the Fengyuan Yang group at The Ohio State University.

4.2.2 Structure and morphology characterization

Fig. 4.2 (a) shows a HAADF-STEM image of a few GaAs/AlGaAs nanowires, where the bright dots at the tapered end of nanowires are Au catalysts. A closer look at the region just under the Au catalysts (Fig. 4.2 (b)) reveals a high density of stacking-fault type defects near the tip. EDS mapping of the GaAs/$Al_{0.35}Ga_{0.65}As$ nanowires in Figs. 4.2 (c) – (f) shows the following: (1) As is uniformly distributed in the whole core/shell nanowires; (2) Ga has a higher concentration in the core region starting at ~100 nm below the Au; (3) Al is concentrated in the ~100-nm section below the Au and in the thin 15-nm shell, as expected; 4) Au is only found at the end of the nanowires. First, the EDS mapping confirms

the designed composition distribution of the core/shell structure. Second, it demonstrates that during the epitaxial growth of the 15nm AlGaAs shell on the side wall of the core GaAs nanowires, AlGaAs also grows through the Au, yielding high stacking fault density and the tapered shape near the Au particle. Figure 2(g) shows a probe corrected HAADF-STEM image projected down a $\{1\bar{1}0\}$ plane of a GaAs nanowire inside a thin AlGaAs shell where the GaAs dimer structure is clearly resolved. The nanowire exhibits zinc-blende crystal structure with a clear stacking fault. The inset to Fig. 4.2 (g) highlights the zinc-blend ABCABC stacking sequence at both sides of the stacking fault, while the two sides are mirror image of each other about the fault line.

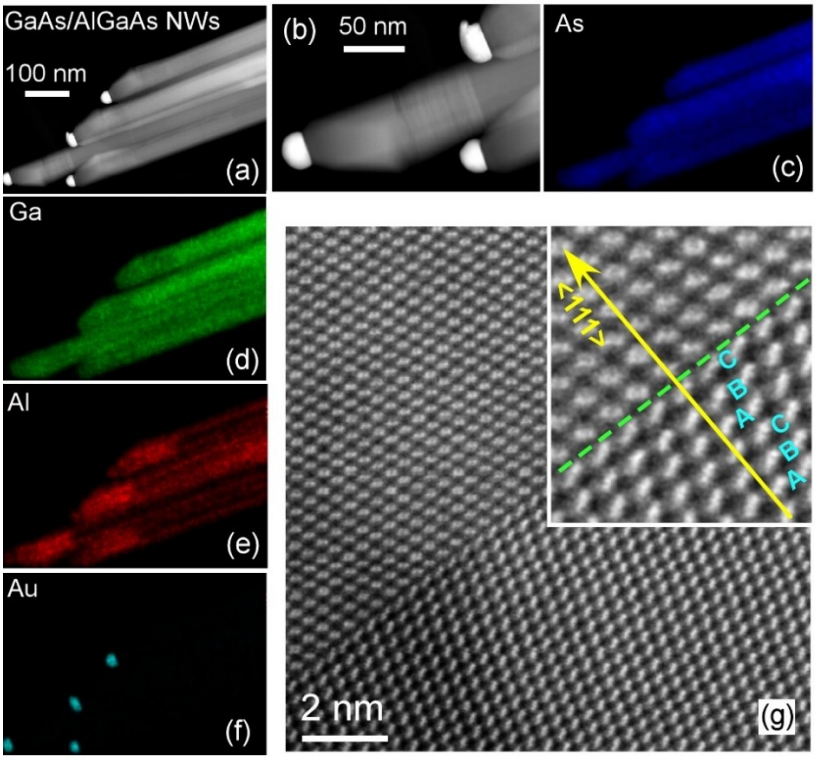

Fig 4.2 (a) Image corrected HAADF-STEM image of four GaAs/AlGaAs core/shell nanowires, (b) zoom-in view near the Au catalysts, and the corresponding EDS maps of (c) As, (d) Ga, (e) Al, and (f)

Au highlighting the distribution of each element. (g) Probe corrected HAADF-STEM image of the core GaAs nanowire shows the zinc-blende crystal structure with the ABCABC sequence of atomic planes along the nanowire axial axis <111>, where the plane sequence forms a mirror image about a stacking fault (green dashed line).

Scanning electron microscope (SEM) imaging was performed using an FEI Helios Nanolab 600 SEM. High angle annular dark field scanning transmission electron microscopy (HAADF-STEM) images and energy-dispersive x-ray spectroscopy (EDS) maps were acquired using an FEI Image-Corrected Titan^{TM} 60-800 scanning transmission electron microscope (STEM) equipped with Super EDX^{TM} as well as an FEI Probe-Corrected Titan^{TM} 80-300. Nanowire growth rate was estimated by measuring 30 or more nanowires from each SEM image to obtain an average length. We note that the reported growth rates were deduced from the wire length and are without the correction for nucleation time, which can be different for wires grown on different substrates.

4.2.3 Photoluminescence studies

Photoluminescence (PL) is an effective way to characterize the optical quality of semiconductor nanowires grown at various temperatures. In this study, PL spectra are excited with a Nd:YVO_4 continuous-wave laser with wavelength $\lambda = 532$ nm, power of 8.1 mW, and spot size of 100 μm. They are measured at 5 K using a 0.3 m spectrometer with a LN_2-cooled back illuminated CCD detector. In order to avoid parasitic luminescence from the GaAs substrate, the nanowires are transferred onto a silicon wafer by gently rubbing the sample across the surface. Measurement of multiple nanowire ensembles

provides insight into the collective spectral quality of the ~10^8 wires grown per substrate per core growth temperature. To avoid oxidation of the AlGaAs shell, all spectra were collected within 24 hours of growth and samples were stored in a nitrogen environment between growth and measurement. Our PL measurements indicate that aging does not impact the PL within one month of growth under our storage conditions.

Fig. 4.3 shows the PL spectra of GaAs(40 nm)/AlGaAs (15 nm) core-shell nanowires grown on GaAs (100) and (111)B substrates with the growth temperature of GaAs core wires varied between 410°C and 472°C. While a sharp band edge emission centered at 819 nm[94] is observed at growth temperatures between 410°C and 430°C for wires grown on (100) substrates, 430°C is the optimal temperature for band edge emission for wires on the (111)B substrate. This dominance of band edge emission in PL is an indication of high optical quality and low defect density, i.e., the dominant recombination mechanism is band edge luminescence rather than defect mediated or non-radiative recombination. As the growth temperature deviates from that of optimal band edge luminescence, wires on both substrates show a red shift in the spectral weight from the band edge emission at 819 nm. A broad peak centered at 830 nm is commonly associated with carbon impurities in GaAs thin films and nanowires grown by MOCVD[92,95,96]. Such a peak is found here in nanowires grown at higher temperatures.

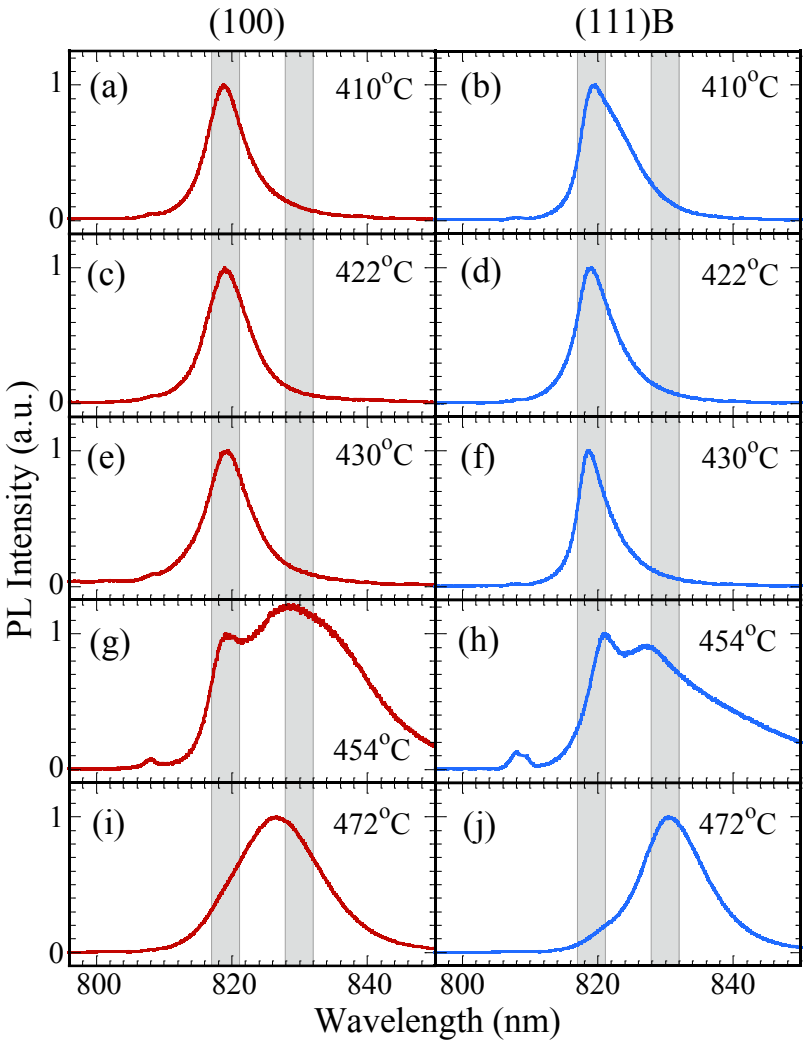

Fig 4.3 PL spectra measured at 5 K for 40-nm GaAs NWs with a 15-nm AlGaAs shell at NW growth temperature of (a) (b) 410°C, (c) (d) 422°C, (e) (f) 430°C, (g) (h) 454°C, and (i) (j) 472°C on GaAs (100) (left column) and (111)B (right column) substrates. While a sharp band edge emission centered at 819 nm is observed at growth temperatures between 410°C and 430°C for wires grown on (100) substrates, 430°C is the optimal temperature for band edge emission for wires on the (111)B substrate.

The observation of enhanced defect luminescence at the high temperature end of our growth window (450 °C – 472 °C) in Fig. 4.3 is likely a result of an increase in sidewall growth with increasing growth temperature. When the growth temperature increases, a shift from VLS to a thin film growth mode induces sidewall growth, leading to a decrease in the axial nanowire growth rate.[88,96,97] Furthermore, in a related case where the growth rate is controlled by V/III ratio rather than growth temperature, Joyce *et al*[93] showed that higher sidewall growth rates of GaAs/AlGaAs NWs are correlated with higher defect incorporation. Figs. 4.3 (a) and (b) show the axial growth rates of the GaAs/AlGaAs nanowires. The overall trend in growth temperature is in general agreement with those reported in the literature[88,98]. The temperature regime where increased sidewall growth reduces the axial growth rate agrees well with that of the enhanced defect luminescence, both occurring at the regime of 450 – 472°C, suggesting the sidewall growth as a potential origin of defect luminescence. We note that the temperatures of maximum growth rate, 440°C to 450°C for both substrates, are 10°C to 20°C lower than those reported by both Borgström *et al.* and Fortuna *et al*.[88,98]. This difference may be due to an offset among different pyrometry systems.

The PL intensity ratio, I_{819nm}/I_{830nm}, is calculated by integrating the photoluminescence at 819 nm and 830 nm with a bandwidth of 4 nm (grey areas in Fig. 4.3), as shown in Figs. 4.4 (c) and (d). Since PL is measured on transferred nanowires to eliminate the substrate signal, the nanowire density varies and relative intensities cannot be immediately compared. This relative strength of the 819 nm band edge peak compared to the 830 nm defect peak provides a density independent measure of nanowire optical

quality. On both substrates, the peak ratios exhibit sensitive dependence on the growth temperature. In the high temperature regime, decreasing the growth temperature decreases the defect peak around 830 nm hence increasing the peak ratio on both substrates. This observation is consistent with the prior discussion and are attributed to the dominance of the VLS growth mode over sidewall growth, leading to reduced defect states in GaAs. In contrast, the peak ratios at temperatures below the maximum growth rate exhibit opposite trends on the different substrates. The 830 nm intensity in this region can still be understood as a benchmark for defect intensity, but does not necessarily correspond to the same defects found in the high growth temperature case.

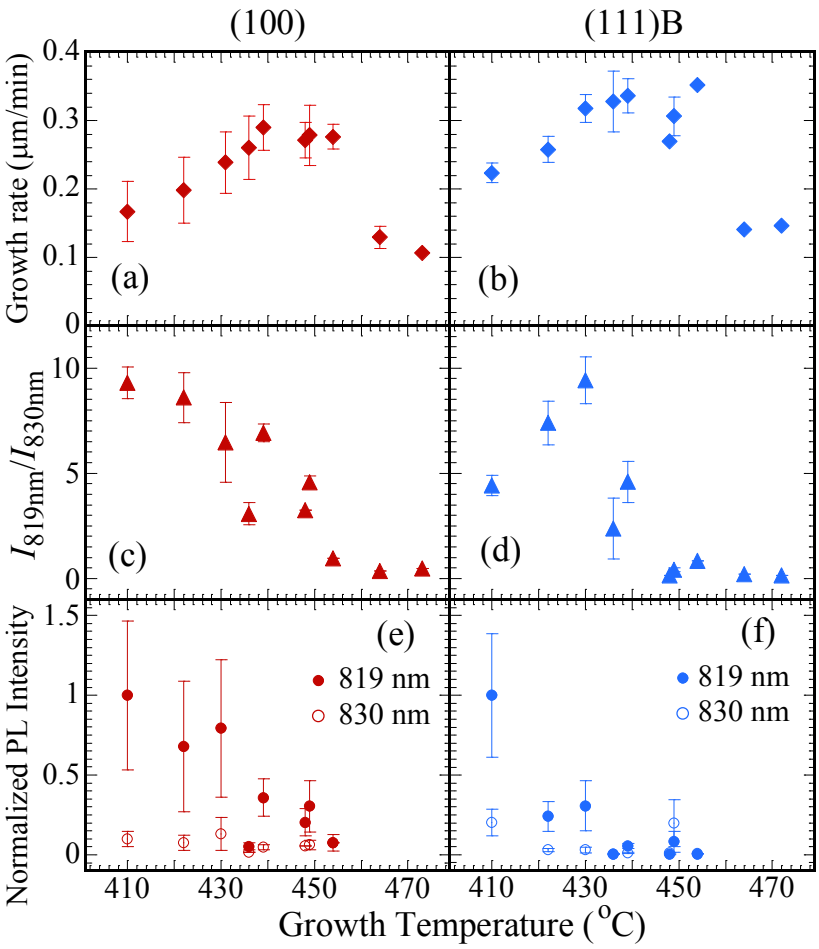

Fig 4.4 Growth rate as a function of the substrate temperature for nanowires grown on (a) GaAs (100) (left column) and (b) GaAs (111)B (right column) substrates. The error bars are one standard deviation from 30 or more nanowires. (c) (d) Ratio of integrated intensities of the 819 nm band edge peak (I_{819nm}) to the 830 nm defect peak (I_{830nm}) with a bandwidth of 4 nm. (e) (f) Normalized PL intensity of both the band edge (solid diamonds) and the 830-nm defect peaks (open circles) as a function of the growth temperature.

To further understand these different trends at lower growth temperatures, an estimate of the average sample density was made and used as an approximate weighting factor for comparison across transferred samples. The resulting normalized PL is shown

in Figs. 4.4 (e) and (f). Fig. 4.4 (e) shows the band edge PL for the (100) grown wires improves with decreasing growth temperature from 450°C to ultimately level off in the 410 – 430°C range. The intensity of the defect peak largely remains constant from 450°C down to 410°C. Hence, those wires grown between 410°C and 420°C exhibit the most band edge dominant PL spectra (Fig. 4.4 (c)). Fig. 4.4 (f) shows the band edge intensity of the (111)B grown wires also grows with decreasing growth temperature from 450°C. In this case, however, the defect intensity becomes stronger from 440°C down to 410°C. As a result, the PL spectra of wires grown at 430°C are the most band edge dominant while those grown at lower temperatures show increasing defect emission (Fig. 4.4 (d)). For further comparison, the (100) wires at 410°C as well as the (111)B wires at 430°C both have a full-width-at-half-maximum (FWHM) of $\lambda_{FWHM} \approx 7$ nm corresponding to FWHM of energy, $E_{FWHM} \approx 13$ meV.

These results identify a substrate-dependent window in the core growth temperature where defects that degrade optical quality may be minimized. In particular, the sensitive dependence of optical characteristics on the growth temperature indicates the importance of optimizing growth temperature in order to prepare high quality GaAs/AlGaAs NWs, as a difference of 10 °C could have considerable impact. Additionally, the substrate dependence originating from defect incorporation suggests that the growth dynamics are not independent of the starting substrate. Although the nanowires grow in the <111> direction on both substrates, the starting substrate and NW geometry play a critical role on the precursor diffusion and subsequent defect density. These results provide insights and directions for future studies on VLS growth dynamics of III-V NWs.

In summary, we have studied the effect of growth temperature on the optical characteristics of GaAs/AlGaAs core/shell nanowires grown on (100) and (111)B GaAs surfaces. PL analysis reveals increased defect density in growth temperatures of 450 ºC - 470 ºC, where the GaAs sidewall growth on the core begins to increase. Below this, defect incorporation differs depending on the orientation of the GaAs substrate. At lower growth temperatures, wires grown on a (111)B GaAs substrate exhibit stronger defect emission in their PL spectra than do those grown on a (100) substrate. This work presents a systematic study that reveals the correlation between the growth temperature of the GaAs core, the chosen substrate surface orientation, and the resulting optical properties of GaAs/AlGaAs NWs. A substrate-dependent window in the core growth temperature can be identified that minimizes defects that degrade optical quality. Future studies of microscopically-resolved PL will allow direct comparison of individual nanowire PL intensity as a function of growth conditions. In conjunction with STEM imaging of a single nanowire will facilitate highly spatially resolved PL data that would yield correlations between specific crystallographic defects and a particular spectral feature.

4.3 Control of optical polarization anisotropy

4.3.1 Polarization-resolved PL measurement

PL spectra are excited with a Ti:sapphire laser operating at continuous-wave mode with wavelength λ = 780 nm, power of 112 mW, and spot size of ~50 μm. To measure the polarization anisotropy, a Glan-Laser linear polarizer is placed in the pump path and a second Glan-Thompson linear polarizer and an achromatic half-waveplate are placed in the collection path. The measurement of the polarization of the nanowire luminescence is realized by keeping the excitation and detection linear polarizer at S polarization and rotating the half-wave plate. For the experimental setup, please refer to Section 2.3. The spectral resolution is provided by a 0.3 m spectrometer and a liquid N_2 cooled CCD camera. The nanowire ensembles are maintained at a temperature of 5 K to maximize PL intensity.

4.3.2 Polarization control in GaAs/AlGaAs core-shell NW

The core-shell structure along with a small mismatch in dielectric constants (ε_{GaAs}:ε_{AlGaAs}= 10.89:10.07), in GaAs/AlGaAs NWs conveniently allows for the control of optical polarization anisotropy in this system. Here, the dielectric matching is realized by engineering the shell thickness to be close to the characteristic length scale, the excitation wavelength and PL wavelength of the system (690 nm and 820 nm, respectively).

Nanowires used in this study are synthesized following similar MOCVD procedures as described in section 4.2.1, with the exception that 30-nm Au colloid suspension is used as the catalyst. The thermal couple temperature for the GaAs core growth is 549.4ºC. AlGaAs shell deposition time is 3 minutes and 15 minutes for a thin

shell and a thick shell sample, resulting in a shell thickness of around 20 nm and 500 nm, respectively. After the growth, nanowires are mechanically transferred to a SiOx (x~2) substrate for optical measurements. The samples studied in this work is synthesized by Nicholas Minutillo from the Fengyuan Yang group at The Ohio State University.

A characteristic PL spectrum of thin-shell GaAs/AlGaAs nanowires is shown in Fig. 4.5 (a). The luminescence centers at 819 nm, corresponding to the bandedge emission of GaAs[94], and exhibits a polarization anisotropy of $\langle\rho\rangle$ = 0.72.

As shown in Fig. 3.7, the polarization anisotropy is found to be reduced from $\langle\rho\rangle$ = 0.72 to $\langle\rho\rangle$ =0.031 in the thin and thick shell sample, respectively (a 96% suppression). A noticeable spectral shifts from 816.9 nm (thin shell) to 820.0 nm (thick shell) indicates influences of the AlGaAs shell on the optical processes in GaAs core. While a detailed investigation into this spectral shift is beyond the scope of this study, a plausible explanation is that tuning the thickness of the AlGaAs shell affects the surface states on the core. As a result, carrier recombination pathways (the recombination with surface trap states, in particular) are modified, therefore giving rise to an overall PL spectral shifts.

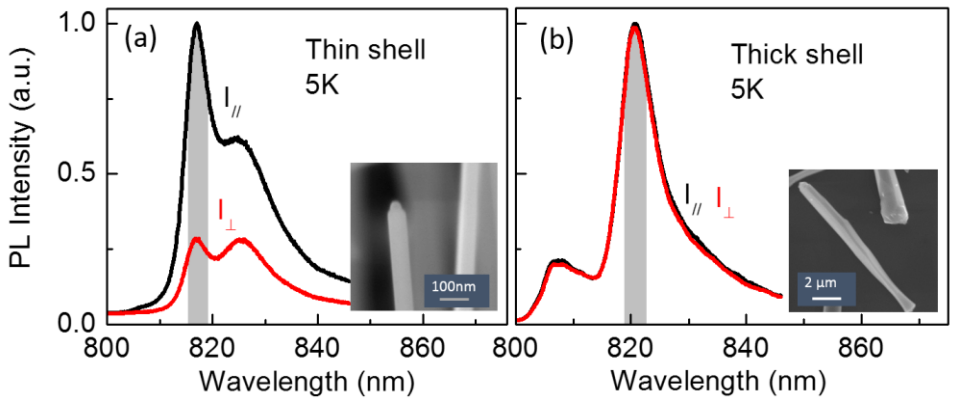

Fig 4.5 (a), (b) Photoluminescence for thin shell and thick shell GaAs/AlGaAs core-shell nanowires, respectively. Inset: corresponding SEM images. The black (red) curves are for excitation polarization parallel (perpendicular) to the detection polarization.

To further explore this polarization anisotropy, a full angular dependence of the normalized PL intensity is measured in thin shell (black squares in Fig. 4.6) and thick shell (blue squares in Fig. 4.6) GaAs/AlGaAs core-shell nanowires. The PL intensity shows a clear cos(2θ) dependence and confirms that the suppression in anisotropy (from $\langle\rho\rangle = 0.72$ to $\langle\rho\rangle = 0.031$) extends for all values of θ. The curves calculated from Eq. (2) are plotted as grey and light blue lines for thin-shell and thick shell nanowires, respectively. Interestingly, the thin shell nanowires exhibit a stronger polarization anisotropy than that predicted from the dielectric model ($\langle\rho\rangle = 0.72$ and 0.43, respectively), likely due to a partial alignment of the transferred nanowire ensembles. The small deviation from the calculated value for the thick shell is approaching the experiment resolution. Given that no free parameters are used in this calculation, the experimental and calculated curves are in good agreement and a successful suppression in polarization anisotropy is demonstrated.

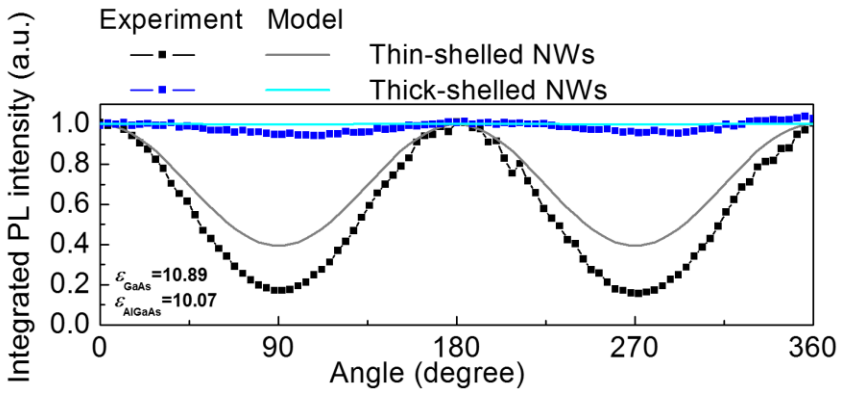

Fig 4.6 Comparison between the experimental (black squares and blue squares) and calculated (grey and light blue lines, see Eq. 2 in section 4.1) normalized PL intensity for thin shell and thick shell nanowire ensembles, respectively.

4.4 Initial attempts to probing spin dynamics in semiconductor nanowires

4.4.1 Challenges in optical spin study of semiconductor nanowires

The suppression of the optical polarization anisotropy in the dielectric-matched GaAs/AlGaAs core-shell NWs (Section 4.3) is a first step toward the optical investigation of 1D spin physics. By engineering an appropriate shell thickness, the core-shell structure simultaneously eliminates the surface defect states of the core nanowires and the large optical polarization anisotropy between excitation parallel and perpendicular to the nanowire axis. Despite this success, further technical challenges remain to be addressed. First, the mechanical transfer technique becomes challenging when the shell thickness approaches around 0.5 μm. At this thickness, a coalesced AlGaAs layer starts to form at the bottom of the nanowires, making them difficult to rub off. This difficulty in turn imposes a constraint on the shell thickness, which is undesirable and limits the degree of dielectric matching that can be achieved. Consequently, another method needs to be

developed to allow for optical access to the GaAs/AlGaAs nanowires while excluding the signal contamination from the underlying GaAs substrate.

Second, AlGaAs shells prepared in the above-mentioned growth mode naturally have a non-uniform thickness (Fig. 4.3 (b)), leading to incomplete suppression of the polarization anisotropy across the wires. The non-uniformity of the shell thickness arises from the shadowing effect from the nanowire forests, which limits the precursor flow at the bottom region of the nanowires and reduces the shell thickness. A complete halt of the shell growth can occur at the bottom of the wires if the shell on the top reaches a thickness where a coalesced AlGaAs layer starts to form. The details of the shadowing process sensitively depend on the spacing and the thickness of the nanowires, as well as the specific growth parameters, such as the growth temperature and the precursor flow. A growth regime that minimizes the shadowing effect needs to be identified in order to provide a uniform dielectric-matching.

Lastly, the dielectric-engineering results in a wire thickness comparable to the wavelength of the laser (of around 1 μm and 818 nm, respectively), making the wires act as effective scattering centers. As a result, severe light scattering hinders optical measurements on these wires.

4.4.2 A proposed sample geometry

In order to address the aforementioned difficulties, we propose a sample geometry based on the GaAs/AlGaAs core-shell nanowires. (Fig. 4.7). A few key characteristics of this sample structure are discussed below.

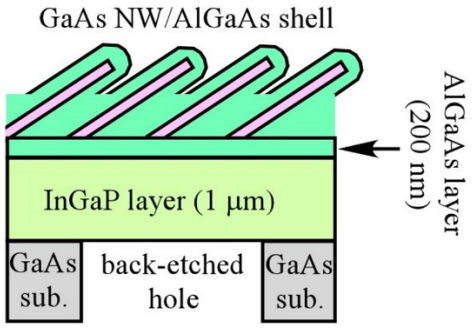

Fig 4.7 A GaAs/AlGaAs NW-based membrane geometry designed for optical spin studies.

1. A latticed-matched InGaP layer is introduced between the GaAs (100) substrate and nanowires. The composition of the InGaP ($In_{0.48}Ga_{0.52}P$) is chosen carefully to be lattice matched with GaAs. Mostly importantly, it serves as a stop layer for the chemical etch that removes the GaAs substrate.
2. The GaAs substrate is etched to open a hole with a diameter of several mm in the back as illustrated in Fig. 4.7. The etching is stopped by the InGaP layer. This suspended nanowire membrane structure offers an alternative way to optically access the nanowires without the thickness constraints as in the case of the mechanically transferred wires.
3. The wire density is reduced in order to achieve a thicker shell deposition and the formation of a coalesced AlGaAs layer at the bottom of the nanowires. The coalesced region is expected to provide ideal dielectric matching and reduces light scattering.
4. Time-resolved Kerr rotation measurements (reflection) are performed from the back of the etched hole in the GaAs substrates (Fig. 10b). The key advantage of this

geometry is that the InGaP surface at the back is exceptionally smooth (determined by the roughness of commercial GaAs substrates). There will be no scattering caused by roughness up to the top surface of the AlGaAs layer.

To realize this sample structure, an $In_{0.48}Ga_{0.52}P$ layer is grown on a GaAs (100) substrate, followed by the deposition of an $Al_{0.35}Ga_{0.65}As$ layer at a substrate temperature of 650°C by MOCVD. The InGaP layer has a perfect lattice match with GaAs and serves as a stop layer for the chemical etch[53]. The $Al_{0.35}Ga_{0.65}As$ layer provides an epitaxial template for the later core-shell nanowire growth. Both $In_{0.48}Ga_{0.52}P$ and $Al_{0.35}Ga_{0.65}As$ layers have larger band gaps than GaAs. Consequently, the bilayers are transparent for the pump and probe light at the wavelength $\lambda \sim 818$ nm corresponding to the band gap of GaAs nanowires. Au catalyst of 40 nm in diameter is diluted (catalyst solution: DI water = 1:10 in volume and dispersed on the GaAs (100) substrates with $Al_{0.35}Ga_{0.65}As/In_{0.48}Ga_{0.52}P$ bilayers, followed by a growth of $GaAs/Al_{0.35}Ga_{0.65}As$ core-shell nanowires. The resulting nanowires with thick shells are shown in Fig. 4.8. The cross-sectional SEM image in Fig.4.8 (b) indicates that a continuous $Al_{0.35}Ga_{0.65}As$ layer of ~500 nm thick is formed during the shell growth. Ideally, the $Al_{0.35}Ga_{0.65}As$ shells will be thick enough to completely fill the space between the GaAs nanowires. For this experiment, we fabricate core-shell nanowire samples with GaAs nanowires embedded in a thick $Al_{0.35}Ga_{0.65}As$ layer of ~2 μm thick (instead of ~500 nm as shown in Fig. 4.8 (b)). A hole is opened in the GaAs substrate by covering the back of the substrate with Crystalbond and exposing an area with a diameter of several mm for citric-acid based selective wet[53].

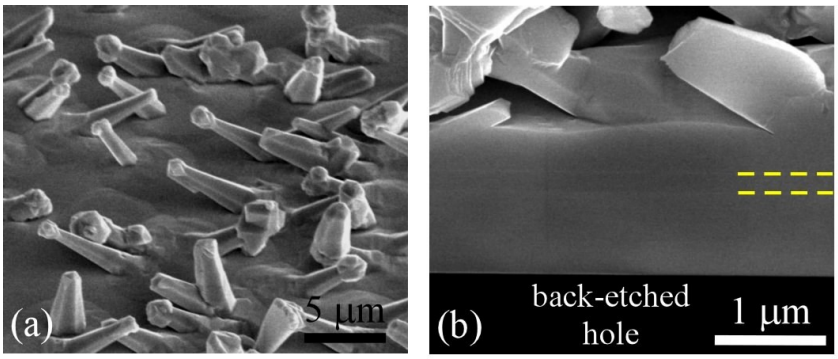

Fig 4.8. (a) SEM image of 40 nm GaAs nanowires with a 500-nm thick $Al_{0.35}Ga_{0.65}As$ shell grown by MOCVD on $Al_{0.35}Ga_{0.65}As$(200 nm)/$In_{0.48}Ga_{0.52}P$(1 μm) epitaxial bilayers which were deposited on a GaAs (100) substrate in a previous MOCVD growth. Part of the GaAs (100) substrate of the core-shell nanowire sample in (a) was selectively etched from the back down to the InGaP layer which serves as an etch stopper. (b) SEM cross-sectional view of the back etched sample at a tilt angle of 52°. The yellow dashed lines in (b) mark the 200 nm AlGaAs layer.

4.4.3 Spin lifetime measurements

Before conducting spin lifetime experiments, PL measurements are first performed from the front and back side of the sample to characterize the optical quality of the fabricated NWs. PL spectra are excited with a mode-locked Ti:sapphire laser with pulse width = 100 fs, wavelength λ = 818 nm, power of 108 mW, and spot size of 50 μm, and measured at 5 K using a 0.3 m spectrometer with a LN_2-cooled back illuminated CCD detector.

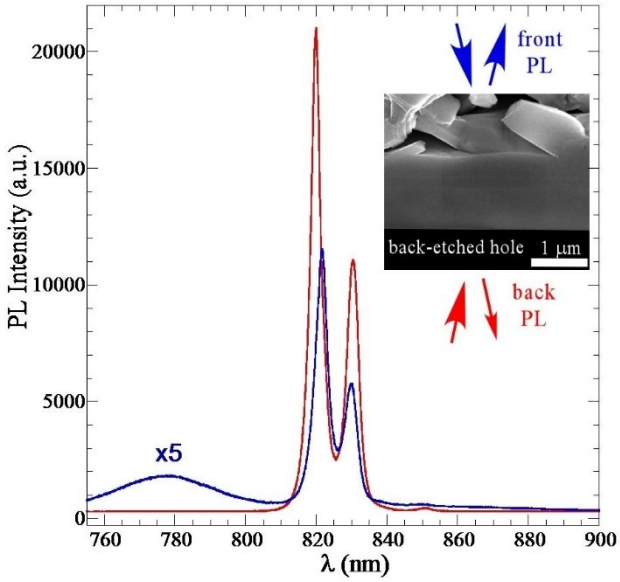

Fig 4.9 PL spectra of GaAs/$Al_{0.35}Ga_{0.65}As$ core-shell nanowires grown on $Al_{0.35}Ga_{0.65}As/In_{0.48}Ga_{0.52}P$ bilayers on a GaAs(100) substrate as shown in Fig. 4.8 (b). The red curve is the PL measured from the front of the sample and the blue curve (intensity magnified by ×5) is the PL taken from the etched hole in the back.

A considerable improvement in the quality of the PL is observed for the PL taken from the back hole, as shown in Fig. 4.9. First, the brightness of the PL measured from the back (red) is about 10 times higher than the one from the front (blue). There are two possibilities for this difference: one is that the GaAs nanowire quality near the substrate is better than the part near the top where Au catalysts are located; the other is the significant scattering from the top surface reduces the intensity of PL collected by the detector. In addition, there is a broad peak at λ = 778 nm for the PL spectrum from the front. For the PL from the back, there are only two expected PL peaks at λ = 820 nm and 826 nm,

originating from the GaAs band edge emission and Si dopant states, respectively. The 778 nm peak most likely comes from the defect states in the $Al_{0.35}Ga_{0.65}As$ grown around the Au nanoparticles (non-epitaxial). Clean PL with minimal defect states (in both core nanowire and shell) from the back of the etched hole indicates the high quality of the core-shell nanowires. This is highly desirable for long spin relaxation time in the nanowires and TRKR measurements of spin relaxation.

Characterization of spin dephasing time is performed by TRKR measurements, which measures the inhomogeneous spin lifetime commonly referred to as T_2^*. The TRKR time trace is acquired at a temperature $T = 5$ K and an applied field $B = 1$ T. Laser pulses of 100-fs duration and 76 MHz repetition rate are generated by a mode-locked Ti:Sapphire laser, and are split into pump and probe pulse trains whose time delay, Δt, is controlled by a mechanical delay line. The pump and probe power ratio is ~27, and the averaged pump power density is 917 W/cm^2.

Unfortunately, the initial TRKR experiments reveal no time-resolved spin signal in the fabricated nanowire membrane. (right panel of Fig. 4.10 (a)) A spike at zero delay is associated with a coherent artifact when both pump and probe hit the sample simultaneously. In diagnosing this failure, a control sample is fabricated, consisting of a bulk GaAs epilayer grown on similar InGaP stop-etch layer. Thickness of the InGaP layer has been reduced to 184 nm. In this sample, the coherent spin precession in the GaAs epilayer is clearly visible, signified by the oscillatory behavior in the TRKR trace (Fig. 4.10 (b)). This result identifies two suspects for the lack of spin signal in the nanowire system. One is the thickness of the InGaP layer. Even though the excitation light is

nominally sub-bandgap for InGaP, the presence of residual absorption due to defects or the tail of the band edge apparently suppresses our excitation over the 2 μm path length (1μm in and 1 μm out). The other likely culprit is the nanowire density. The nanowire sample has a lower absorption cross section compare to the GaAs control, as there is less material to interact with light. This can lead to a reduced TRKR signal and therefore difficulty in the detection.

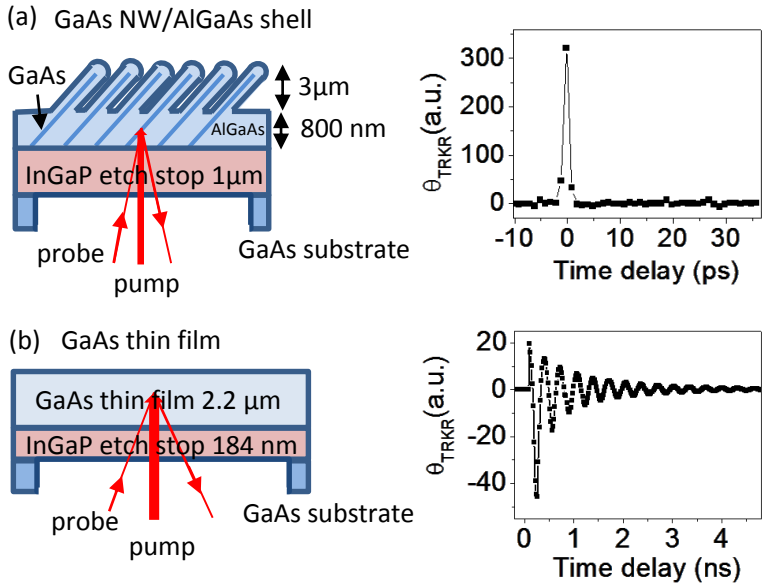

Fig 4.10 (a) Left panel: schematic of the NW sample structure and the TRKR measurement geometry. Right panel: time-resolved Kerr rotation (TRKR) trace measured on the NW sample. (b) Left panel: Schematic of a GaAs thin film control sample and the TRKR measurement geometry. Right panel: TRKR time trace measured on the control sample, showing coherent spin precession.

4.5 Summary and outlook

In summary, a dielectric-matched membrane structure based on GaAs/AlGaAs core-shell nanowires is developed to facilitate optical investigations of spin dynamics in 1D semiconductors. A systematic study of the core growth temperature and substrate orientation in the MOCVD growth identifies a growth window to produce GaAs/AlGaAs nanowires with optimal optical quality. Dielectic matching the GaAs core with the AlGaAs coating proves to successfully eliminate the optical polarization anisotropy, which has been a fundamental obstacle hindering optical access to 1D spins. Toward ultrafast pump-probe study in 1D, a NW membrane structure is engineered that simultaneously addresses the optical polarization anisotropy and other technical challenges. Even though a spin signal is absent in the initial TRKR experiment, a GaAs thin film control lends the validity of the designed sample geometry and identifies the InGaP thickness and nanowire density as the possible suspects for the lack of spin signals. These results serve as a promising starting point and provide useful information toward the ultimate goal of optical investigation of 1D spin physics.

Chapter 5:
Magneto-optical interactions and optical spin orientation in germanane

5.1 Introduction

Since the discovery of single layer graphene in 2003[99,100], two-dimensional (2D) materials have become an active research field which attracts widespread interest. The reduced dimensionality leads to unique properties in 2D semiconductors that are not possible in their bulk counterpart, making them appealing candidates to explore fundamental science and device applications[101–105].

Of particular interest to this dissertation are the spin properties in 2D materials. Due to confinement effects, 2D systems exhibit fascinating and novel properties that are advantageous for spintronics applications[106–111]. For instance, an electron spin polarization of up to 100% can be created in 2D heterostructures by optical orientation, as a result of the lifting of heavy-hole degeneracy[25,112,113]. In MoS_2, the broken inversion symmetry gives rise to the coupling between the valley and spin degree of freedom, allowing for selective excitation of a certain valley through optical excitation[114–116].

In the family of 2D materials, germanane, or hydrogen-terminated germanium (GeH), is a particularly interesting system. It consists of germanium atoms arranged in a buckled honeycomb lattice and surface terminated by hydrogen atoms. The buckling has profound impact on the electronic and chemical properties of germanane[117]. First of all, it

enhances the chemical reactivity, leading to germanane formation via sp^3 bonding and consequently the opening of a direct gap[117] (Fig. 4.2 (b)). The existence of a band gap is advantageous for device applications and in strong contrast with other elemental 2D materials such as graphene, silicene, and germanene, and stanene, which are known to be Dirac cone materials with a linear dispersion at the K point[118] (Fig. 4.2 (a)) and zero bandgap. The direct nature of the band gap also makes germanane optically active, opening up the opportunity for optical investigations and applications.

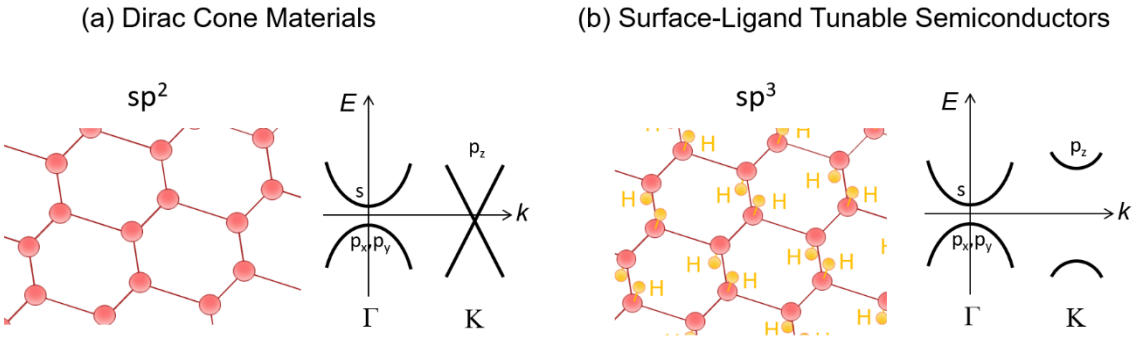

Fig 5.1 Schematic diagram of the crystal structure (let panel) and band structure (right panel) of the Dirac cone materials (a) and surface-ligand tunable semiconductors (b).

In addition to the band gap, the buckling-induced sp^3 bonding also results in high surface sensitivity in germanane, which hasn't been achievable in many other 2D van der Waal materials, such as graphene, because the favored sp^2 bonding renders them relatively inert. Consequently, germanane holds great promise for band engineering via covalent chemistry. It is predicted that by varying the surface termination in the sp^3 bonds, it would be possible to manipulate the band gap, band alignment, thermal stability, and spin-

dependent interactions[103,119]. Experimentally, replacement of the hydrogen termination in germanane with other ligands, such as methyl ligand, has been shown to impact the electronic structure, resulting in an increase of the band gap and the improved stability[120,121].

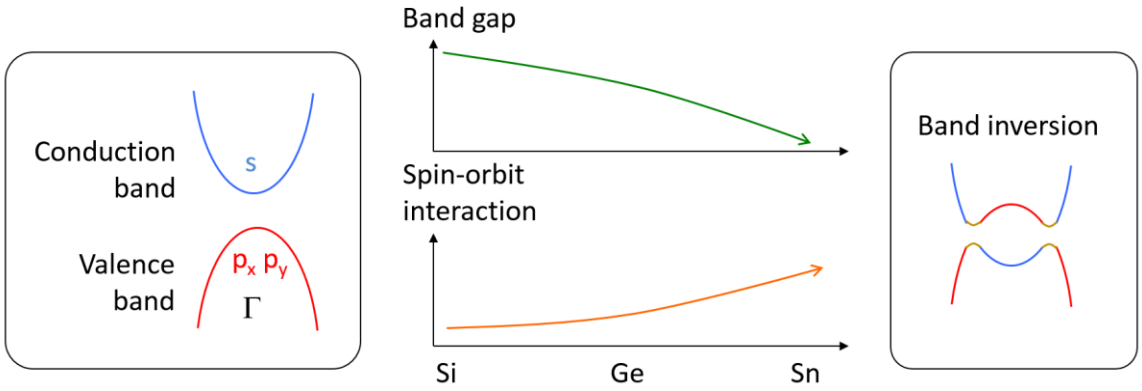

Fig 5.2 Evolution of the size of the band gap and spin-orbit interaction in Si, Ge, and Sn (middle panel). Due to the increasing spin-orbit interaction and the decreasing band gap, a band inversion in 2D is predicted to occur when going down the periodic table of the group IV elements. (left and right panel).

For spintronics research, germanane has a stronger spin-orbit interaction than graphene. The stronger spin-orbit interaction coupled with the reduced band gap makes germanane a promising candidate for exhibiting an inversed band structure and thus the topological quantum spin Hall (QSH) phase (Fig. 4.2). While the existence of a QSH phase in germanane remains to be explored, various predictions in related 2D buckled elemental materials[107,109,111,122–124] have been made. Similar behaviors could be expected in germanane.

Being a relatively young material (the first successful synthesis of multi-layer germanane was demonstrated by the Goldberger group in 2013[119]), the fundamental properties, such as the band structure, transport, and optical properties, remain to be explored. Here, we present the first study investigating the magneto-optical properties and optical orientation in germanane using continuous wave (cw) luminescence techniques including magneto-PL and circular polarization resolved PL spectroscopy. These results reveal valuable information about germanane and lays the foundation for the future study of spin dynamics using ultrafast pump-probe techniques.

5.2 Sample synthesis

5.2.1 Principle of synthesis

The synthesis of germanane is realized following a two-step route[119,125]. Zintl-phase $CaGe_2$ is first grown as a starting material. It is subsequently immersed in hydrochloric acid (HCl) in order to de-intercalate the Ca atoms to form van der Waals GeH. The resulting crystal structure adopts a stacked layered structure following that of the Zintl-phase $CaGe_2$ and is distinctively different from its bulk form germanium. In this layered structure, each layer is a 2D germanane sheet where Ge atoms are arranged in a buckled honey-comb lattice and covalently bonded to H atoms, as shown in Fig. 5.3.

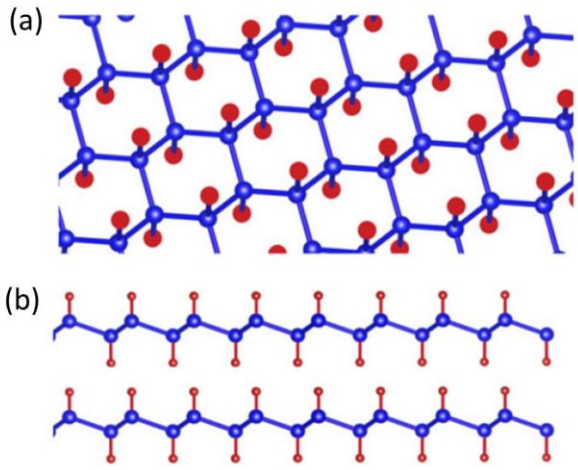

Fig 5.3 (a) Atomic structure diagram of GeH (b) Side view of the stacked layers of GeH. Figure is adopted from Ref [125].

Germanane samples studied in this work are synthesized by "epitopotaxial" growth[125]. This method combines an **epi**taxial molecular beam epitaxy (MBE) growth of $CaGe_2$ on Ge(111) substrate, and a subsequent **topotac**itc HCl transformation to de-

intercalate the Ca atoms. In particular, the $CaGe_2$ is prepared using an epitaxial co-deposition growth, an advanced approach that has been shown to provide improved crystalline quality and thickness control compared to other growth methods.

5.2.2 Synthesis parameters

To synthesize $CaGe_2$, MBE growth is performed in an ultrahigh vacuum (UHV) chamber with base pressure of 2×10^{-10} Torr. Elemental Ge and Ca are evaporated from thermal effusion cells with high purity Ge (99.9999%, Alfa Aesar) and Ca (99.99%, Sigma Aldrich) source materials. Growth rates are determined by a quartz deposition monitor. For the two samples under study (sample A and sample B), the growth time is 333 minutes and 275 minutes, respectively. The targeted $CaGe_2$ thickness for sample A and sample B is 100 nm and 500 nm, respectively.

All films are grown on undoped Ge(111) single-sided polished wafers with an average wafer thickness of 0.35 mm and an orientation tolerance of 0.5° (University Wafer). The starting 2 inch diameter wafer is cleaved into smaller pieces, which then undergo chemical etching to remove surface oxides/metals and replace them with a thin protective oxide film. Etching involves a sequence beginning with submersion into a 10:1 mixture of H_2O:NH_4OH for 60 s followed by 60 s in a 10:1 mixture of H_2O:H_2SO_4. Finally, the substrates are placed into a H_2O_2 solution for 60 s before being rinsed by de-ionized (DI) water and loaded into the UHV MBE chamber. The substrate is annealed at 650 °C for 30 min as measured by a thermocouple located near the substrate. Annealing thermally desorbs the protective oxide from the Ge(111) surface. With the substrate still at 650 °C, a

5 nm, Ge buffer layer is deposited with typical rates of ~2 Å/min as measured by a quartz microbalance deposition monitor. This procedure is followed for all $CaGe_2$ films grown in this study.

The conversion from $CaGe_2$ to GeH is realized by submerging the $CaGe_2$ in 37% HCl at -40 ºC for 24 hours for both samples. X-ray diffraction and Raman spectroscopy confirm that the resulting film is indeed germanane. Atomic force microscopy (AFM) and reflection high energy electron diffraction (RHEED) measurements reveal a smooth local morphology at the atomic scale and a grain size of a few micrometers, primarily limited by the terraces due to the miscut of the Ge substrate.

The samples studied in this work is synthesized by Patrick M. Odenthal from the Roland Kawakami group at The University of California Riverside. More information on the sample characterization can be found in Ref [125].

5.3 Magneto-PL study

5.3.1 PL spectroscopy

Considering the in-direct band gap in bulk germanium and zero gap (Dirac cone) in germanene, the existence of a band gap in germanane is a remarkable feature, making it advantageous for device applications and opening the door for optical investigations. Before attempting the magneto-PL and optical orientation experiments, we discuss first the PL spectrum of germanane and a few relevant aspects associated with it.

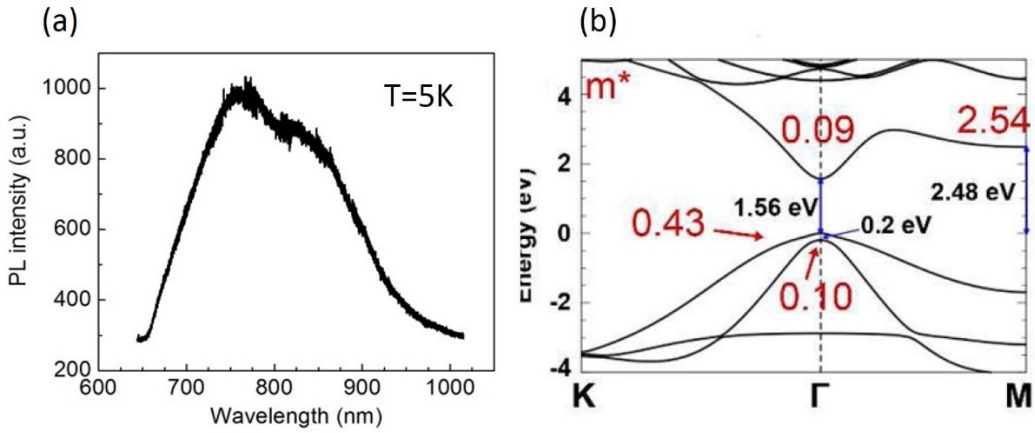

Fig 5.4 (a) 5K PL spectrum of GeH. (b) Calculated electronic band structure of an isolated single layer GeH (data adopted from Ref [119]), showing a direct band gap of 1.56 eV (corresponding to ~795 nm in wavelength) at the Γ point.

The PL measurements uses a helium-neon continuous-wave laser with wavelength λ = 632.8 nm, power of 180 μW, and spot size of 50 μm for excitation. Spectra are measured at 5 K using a 0.3 m spectrometer with a LN_2-cooled back illuminated CCD detector. In order to avoid excitation contamination in the PL detection, a 633 nm notch

filter is included in the detection path. The details of the experimental setup can be found in Section 2.2.

Fig. 5.4 (a) shows a representative PL spectrum of a multi-layer GeH sample. The emission appears as a broad band spanning from 700 nm to 1000 nm. Decay in the PL intensity is commonly observed in these samples over time. The decay rate decreases with decreasing excitation intensity but persists down to the lowest excitation power achievable in our experiment (~10 W/cm^2. The lowest excitation power is limited by the sensitivity of the PL intensity measurement), causing an intensity decay of ~20 %/hr. This decay is further found to be present when the sample is immersed in superfluid helium where the heat generated by the photo excitation is effectively dissipated, suggesting that it originates from laser-induced damage and rather heating effects.

Even though the sample is luminescent, the origin of the luminescence is unclear. We have observed that the luminescence at the shorter wavelength of around 700 nm emerges as time progresses, suggesting a possible correlation with oxidation for PL in this region. A direct band gap of 1.56 eV at the Γ point (corresponding to a emission wavelength of ~795 nm) has been predicted[119], as shown in the calculated electronic band structure in Fig. 5.4 (b). In a recent optical study conducted by Odenthal *et al*[126], GeH samples show a band gap of 1.88 eV (660 nm) at 4.6 K in the absorption spectroscopy, while the PL occurs at 1.45 eV (~855 nm) at 10 K. The samples studied are synthesized using the same growth procedures and apparatus as those in this study.

Clearly, these inconsistent results call for further investigations in order to fully understand and identify the band edge emission in GeH. Nevertheless, three possible

scenarios can be considered for the origin of the observed PL. (1) The band edge of GeH is at 1.56 eV (~795 nm) and the broadness of the PL spectrum is a result of the sample inhomogeneity. (2) The band edge of GeH is at 1.88 eV (660 nm) and the PL originates from exciton luminescence, with a large exciton binding energy of 0.4~0.7 eV. (3) The band edge of GeH is at 1.88 eV (660 nm) and is not observable. The detected PL arises from defect luminescence

While the band edge in GeH and the origin of the observed PL remain an open question, we believe valuable information could still be obtained by studying the magnetic field response of the PL and performing the optical orientation experiments. These results are present in the following sections.

5.3.2 Field dependence of PL

Magneto PL experiments are conducted at 5 K in the Faraday geometry in order to investigate the magneto-optical interactions in germanane. The measurement parameters are the same as those described in Section 5.3.1 with the following modifications: (1) the excitation power is 1.3 mW, (2) polarization optics are included in the excitation and detection beam path as described in Section 2.3, and (3) a magnetic field up to 7 T is applied in the direction perpendicular to the sample plane. The circular polarization CP is obtained using the equation,

$$CP = \frac{I_{\sigma^+} - I_{\sigma^-}}{I_{\sigma^+} + I_{\sigma^-}} \tag{5.1}$$

Here, $I_{\sigma+}$ and $I_{\sigma-}$ represent the PL intensity of the σ^+- and σ^--polarized component.

Emission intensities measured in the circular polarization basis are shown in Fig. 5.5 (a). While there is no difference between the σ^+ and σ^- spectrum ($I_{\sigma+}$ and $I_{\sigma-}$, respectively) at zero magnetic field, a significant intensity difference occurs when a magnetic field of 7 T (and -7 T) is applied, corresponding to a degree of circular polarization up to 18% at 7 T (-18% at -7 T) (Fig. 5.5 (b)).

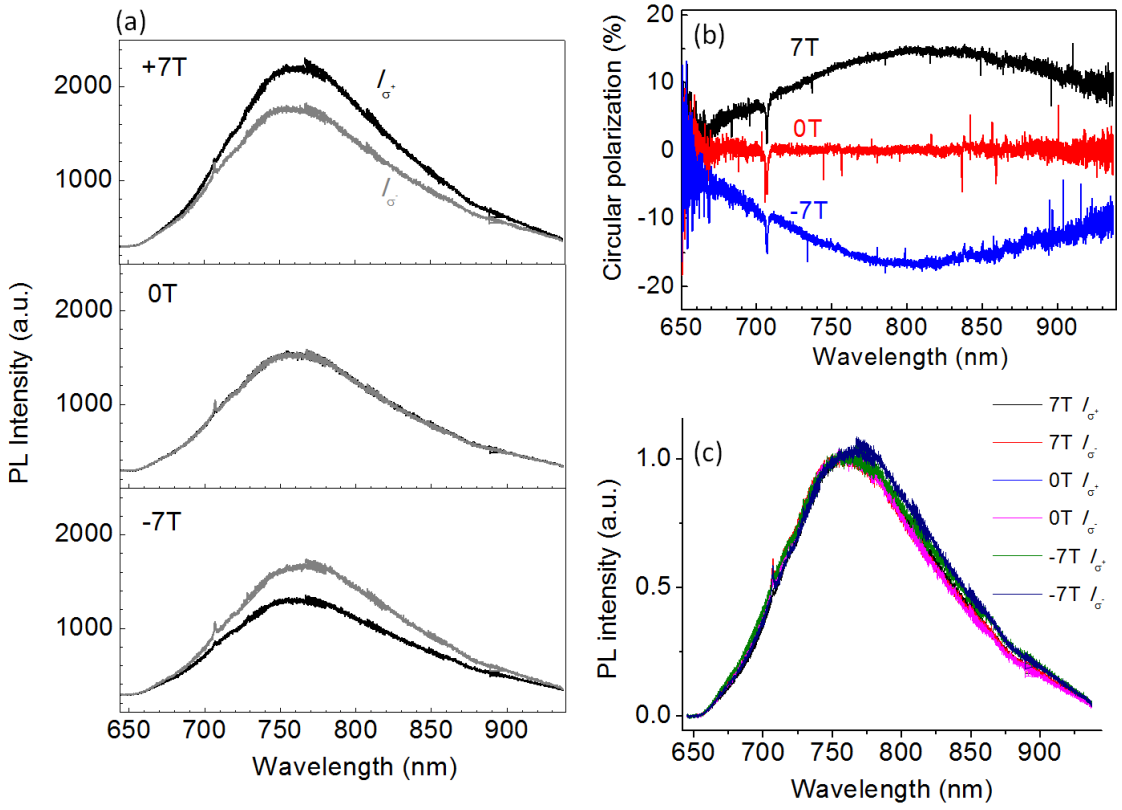

Fig 5.5 (a) Circular polarization-resolved PL spectra of GeH measured at 5 K and an applied field of +7 T (top panel), 0 T (middle panel) and -7 T (bottom panel). (b) Spectrally-resolved circular polarization spectra obtained from data set in (a). (c) Normalized PL spectra obtained from data set in (a).

This large field response in the intensity channel of the magneto-PL spectra is a promising starting point. We discuss additional features as follows. First, the line shape of the PL spectra appears to be insensitive to the applied field, showing no apparent feature of the spectral shifts that one would expect from Zeeman splitting (Fig. 5.5 (c)). Given the broadness of the PL peak, it is not surprising that these fine PL features can't be resolved in the current sample. In addition, the sign of the CP changes when flipping the direction of the magnetic field. This serves as a strong support that the circular polarization of the PL is induced by the applied magnetic field. Furthermore, the field response can be observed over the entire spectral range of the PL spectrum. The maximum of CP occurs at 814 nm, decreasing monotonically when deviating from the maximum.

5.3.3 Field dependence and temperature dependence of CP

To further explore the magneto-optical behaviors in GeH, a magnetic field sweep from -7 T to 7 T is performed. Field dependence of the degree of circular polarization can often serve as a useful probe to the magnetic order of a material. For instance, for a paramagnet, the field dependence of the magnetization can be described by Brillouin functions,

$$M(B,T) = NgJ\mu_B B_J \tag{5.2}$$

where N is the number of atoms per unit volume, g the g factor, μ_B the Bohr magneton, B_J the Brillouin function,

$$B_J = \frac{2J+1}{2J} ctnh\left(\frac{2J+1}{2J}x\right) - \frac{1}{2J} ctnh\left(\frac{x}{2J}\right) \tag{5.3}$$

here J is a positive integer or half-integer. x is the ratio of the Zeeman energy to the thermal energy k_BT.

$$x = \frac{g\mu_B JB}{k_B T} \tag{5.4}$$

This gives rise to a field response where the magnetization grows monotonically with increasing magnetic field until it reaches a saturation value, corresponding to a complete alignment of all the spins. Since the circular polarization measures the average spin, which is proportional to the magnetization, a Brillouin-like behavior is expected to be observed in the circular polarization of the PL.

Fig. 5.6 shows the CP evolution of the GeH PL at 870 nm. Unlike the saturation behavior described by the Brillouin functions, the degree of CP exhibits a monotonic increase with increasing field up to 7T. This clear deviation could be an indication that GeH is not paramagnetic or that the magnetic field energy is insufficient to fully align all the spins at the current field range.

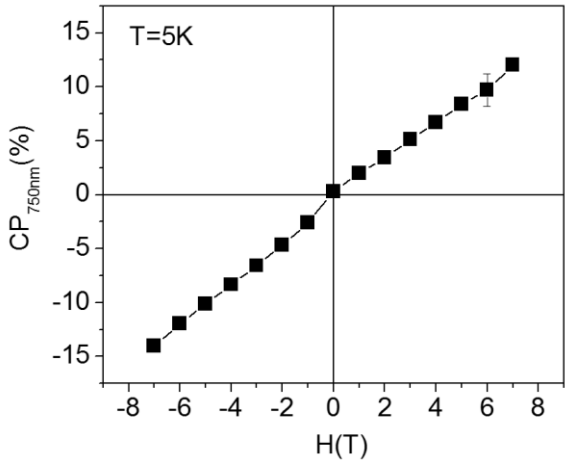

Fig 5.6 Field dependence of the circular polarization of GeH PL measured at 5K. The magnetic field is perpendicular to the sample surface.

Alternatively, one can look at the temperature effect on CP. Since $1/T$ plays a similar role as B in the function form of the Brillouin function (Eq 5.3 and 5.4), the saturation of the magnetization can be achieved by either increasing the magnetic field B, or decreasing the system temperature T. Fig. 5.7 shows a temperature study of CP at 7 T. By varying the temperature, CP as a function of $1/T$ reveals a clear saturation behavior at around 2 K, reaching 19%. A monotonic decrease down to around 0% is observed as the temperature is raised to 100 K. Normalizing the CP curve by the saturation value allows a Brillouin fit with two free parameters, g and J. By fixing J at a fixed value (1/2, 1, and 3/2) and allowing g to vary, excellent agreement between the fits and the experimental data provides strong evidence that the GeH is paramagnet-like. The extracted g factor for each J is indicated in Fig. 5.7 (b). Although a unique determination of g and J are not possible, these results provide insights on the g factor when the circular polarization of the PL are resulted from an electron spin (J=1/2), hole spin (J=1/2 or J=3/2), or exciton spin (J=1).

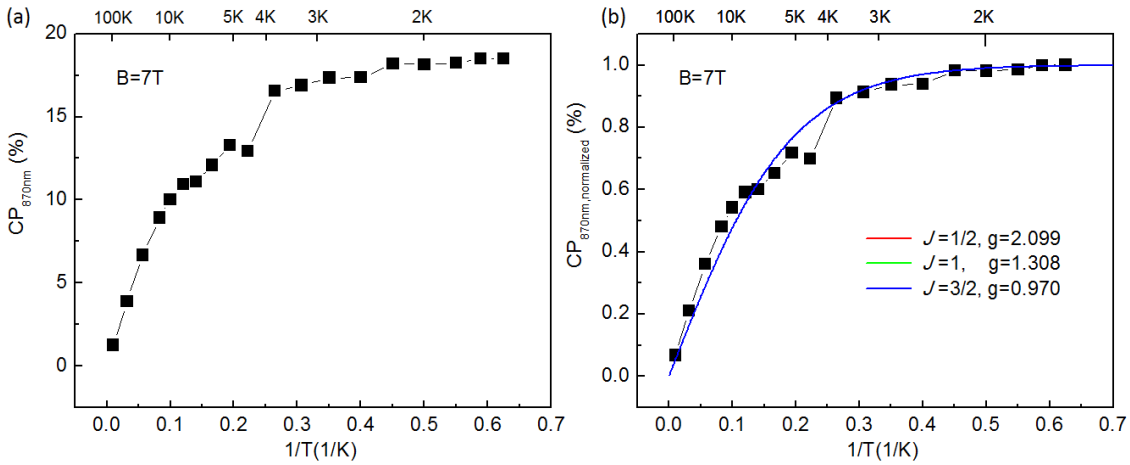

Fig 5.7 (a) Temperature dependence of the circular polarization of GeH PL (b) Normalized CP from data set in (a) (solid squares) and Brillouin fits (solid lines).

5.4 Optical orientation

Optical orientation is the process whereby a net spin polarization is created in a material by a circularly polarized optical excitation (for more information, see Section 2.1). The validity of this process rests on the optical selection rules and the spin orbit interaction. Therefore, optical orientation is of fundamental interest, manifesting the quantum nature of the electron and the band structure. It is also a critical first step toward ultrafast pump-probe spin studies. Here, we present the first optical orientation experiment on GeH.

5.4.1 Optical orientation experiments

The optical orientation experiment is performed at 5 K by excitation of circular polarized light from a helium-neon continuous-wave laser with a wavelength of 632.8 nm, power of 200 μW, and spot diameter of ~50 μm. The preparation of the excitation polarization, the polarization analysis of the luminescence, and the schematic of the experimental setup are described in Section 2.3. The circular polarization CP is obtained by Eq (5.1), and $I_{\sigma+}$ and $I_{\sigma-}$ represent the PL intensity of the co- or counter-circularly polarized component with respect to that of the excitation laser. A 633 nm notch filter is placed in the detection path to suppress the stray light from the excitation.

The polarization-resolved PL spectra are shown in Fig. 5.8. Under $\sigma+$ excitation, the difference between $I_{\sigma+}$ and $I_{\sigma-}$ is not apparent (Fig. 5.8 (a)), but the spectrally-resolved CP spectrum reveals a noticeable degree of polarization of around 3% in the vicinity of 870 nm (Fig. 5.8 (b)). The polarization response is only observable at wavelength longer than 780 nm, corresponding to the long wavelength shoulder in the PL spectra.

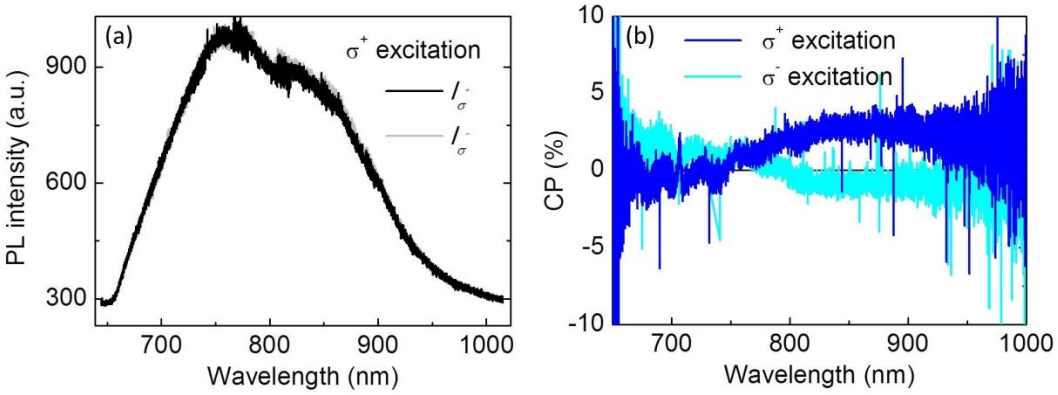

Fig 5.8 Optical orientation in multi-layer GeH at 5K. (a) Polarization resolved-PL spectra ($I_{\sigma+}$ and $I_{\sigma-}$) under $\sigma+$ excitation (b) Spectrally-resolved CP spectra under $\sigma+$ and $\sigma-$ excitation.

The helicity of the excitation is inverted from σ^+ to σ^- to further investigate this polarization signal, leading to an overall sign change in the CP spectrum and a reduced degree of CP from +3% to -0.8% at 870 nm (Fig. 5.8 (b)). The sign reversal and the dependence of CP on the excitation helicity are strong indications that the polarization signal originates from optical orientation. On the other hand, the unexpected asymmetry in the magnitude of the CP could signify a certain asymmetry in the band structure that leads to an asymmetry in the circular polarization channel. A detailed understanding of this phenomenon requires further investigations and is beyond the scope of the current study. This result certainly reveals one intriguing direction for future research on the band structure of germanane or related materials.

As a comparison, the above experiments are repeated under linear excitation. A clear absence of CP signal at wavelength longer than 800 nm is observed for both excitation polarization (*S* and *P*, in this case) (Fig. 5.9). This is in strong contrast to the case with

circular excitation, further supporting that the observed CP in Fig. 5.8 is associated with the optical orientation.

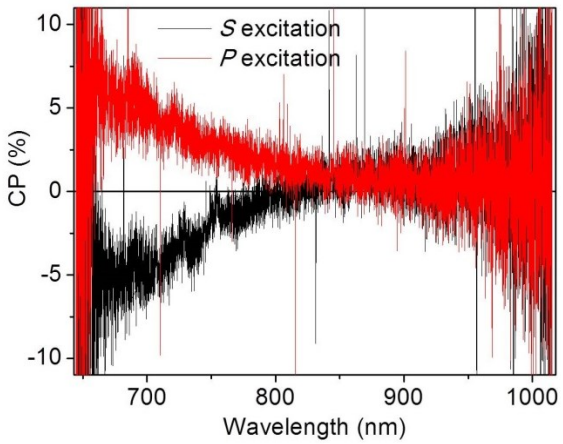

Fig 5.9 Spectrally-resolved CP spectra of multi-layer GeH under linear excitation *S* and *P*.

Next, we look at the excitation power dependence of CP. As the excitation power increases, an optical orientation signal is expected to grow and eventually saturates due to the dominance of the spin-polarized photo-carriers over the un-polarized band carriers. (See Section 2.1 from more information.). A similar increase of CP with increasing excitation power is seen in Fig. 5.10 but the CP continues to grow up to the highest excitation power. While further investigation of the saturation behavior is hindered by the rapid PL decay at high excitation power, the observed power dependence is in general agreement with the nature of the optical orientation process.

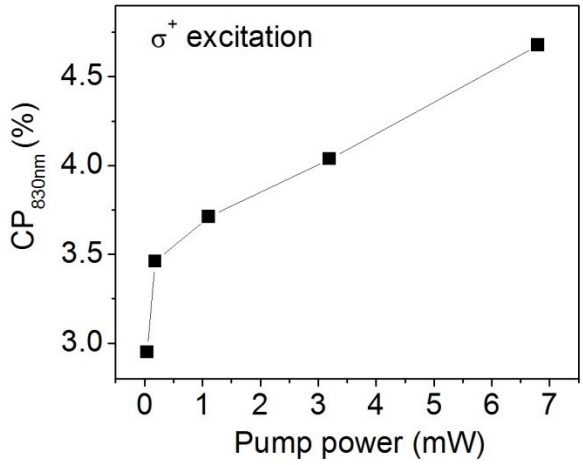

Fig 5.10 Circular polarization of PL at 830 nm as a function of excitation power for a multi-layer GeH sample under $\sigma+$ excitation.

5.4.2 Control measurements

In additional to the studies discussed above examining the various characteristics associated with the optical orientation, control measurements are conducted in an effort to rule out artifacts that could contribute to the circular polarization of the PL.

First, we look at the effect of PL decay, which is a common phenomenon in the GeH samples under study. Since CP measurements are essentially intensity measurements of the two polarization components of the PL, perturbations to the PL intensity could give rise to a finite degree of CP, depending on the nature of the perturbation and the way the CP measurements are conducted. In this study, CP is averaged over 10 data sets, measured back to back. The corresponding PL intensity measurements are carried out in the order of $[(I_{\sigma+}, I_{\sigma-})_1, (I_{\sigma+}, I_{\sigma-})_2, \ldots]$, where each pair of $(I_{\sigma+}, I_{\sigma-})_{i,\ i=1\sim10}$ is used to calculate one CP

spectrum, $CP_i = \frac{(I_{\sigma^+})_i - (I_{\sigma^-})_i}{(I_{\sigma^+})_i + (I_{\sigma^-})_i}$. Considering a simplified case where the sample emits linearly polarized PL (i.e. CP=0), PL decay would then lead to an artificial positive CP because $I_{\sigma^+} - I_{\sigma^-}$ in each CP measurement is nonzero and positive.

To examine if the PL decay contributes to the observed CP signal in Fig. 5.8, a simple trick is to swap the assignment of the two PL polarization components while maintaining the detection order of the polarization component (i.e. always measure I_{σ^+} first, then I_{σ^-}). For a CP signal originating from PL decay, the CP spectrum wouldn't care about the polarization assignment, as the polarization component that is measured earlier (I_{σ^+}) always has a higher intensity than the one that is measured later (I_{σ^-}). Consequently, the resulting CP spectrum will be identical after swapping the polarization assignment. On the other hand, if the CP signal originates optical orientation, swapping the polarization assignment introduces a minus sign to the data, as now the so called $I_{\sigma+}$ is actually $I_{\sigma-}$ and vice versa.

Experimentally, the swapping of the polarization assignment is realized by switching the bias voltage of the variable phase retarder. The bias voltage ($V_{\sigma+}$, $V_{\sigma-}$) applied for detecting (I_{σ^+}, I_{σ^-}), respectively, are changed from (v_1, v_2) to (v_2, v_1). The result is shown in Fig. 5.11. Upon swapping of the polarization assignments, the CP signal changes sign from positive to negative while its magnitude remains roughly constant. This result agrees with the optical orientation mechanism and rules out the suspicion that the PL decay is the dominant source of the observed circular polarization.

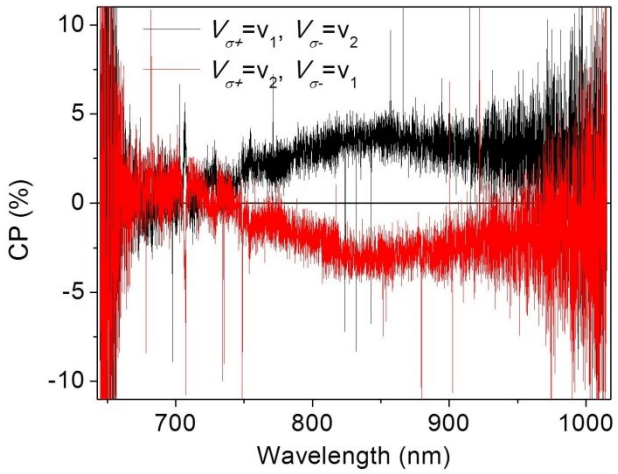

Fig 5.11 CP spectra with reversed assignment of the polarization component of the PL. The bias voltage ($V_{\sigma+}$, $V_{\sigma-}$) applied for detecting ($I_{\sigma}{}^{+}$, $I_{\sigma}{}^{-}$), respectively, are changed from (v_1, v_2) to (v_2, v_1) to test for the effect of PL decay on the CP.

Next, we consider the effect due to the dispersion of the polarization optics. In polarization-resolved PL measurements, polarization optics are usually calibrated at a targeted wavelength in order to eliminate artifacts due to dispersion. Since the band edge emission of GeH hasn't been clearly identified and the PL occurs over a broad wavelength range over 300 nm, it is worth additional attention to examine if the polarization signal is due to the optics dispersion.

The optical orientation experiments are repeated at various different targeted wavelength in order to test for optics dispersion. No significant changes are found in the resulting PL and CP spectra. Fig. 5.12 shows two CP spectra measured at the targeted wavelength of 800 nm and 850 nm. Despite some minimal discrepancy, the overall

behavior and signal magnitude appear insensitive to the targeted wavelength, indicating that the optics dispersion has negligible impact on the CP results.

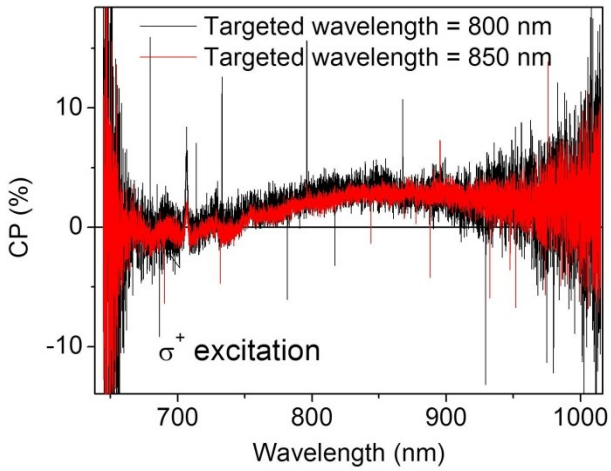

Fig 5.12 CP spectra with two targeted wavelengths for the polarization detection: 800 nm and 850 nm.

5.5 Conclusions and outlook

In summary, magneto-optical interactions and optical orientation are explored in multi-layer germanane (GeH). Magneto-Photoluminescence experiments reveal a strong magnetic field-induced circular polarization up to 18% at 7T and a paramagnet-like behavior with varying temperature. With circularly polarized excitation, a small degree of circular polarization in the photoluminescence (up to 3 %) is achieved, exhibiting the expected helicity and power dependence on the photo excitation. These results of the first magneto-optical and spin orientation study in GeH provide a promising starting point toward future ultrafast pump-probe investigation of spin dynamics.

Bibliography

1. Wolf, S. a *et al.* Spintronics: a spin-based electronics vision for the future. *Science* **294,** 1488–1495 (2001).

2. Wolf, S. a., Chtchelkanova, a. Y. & Treger, D. M. Spintronics-A retrospective and perspective. *IBM J. Res. Dev.* **50,** 101–110 (2006).

3. Žutić, I., Fabian, J. & Sarma, S. Das. Spintronics: Fundamentals and applications. *Reviews of Modern Physics* **76,** 323–410 (2004).

4. Nitta, J. Semiconductor spintronics. *NTT Tech. Rev.* **2,** 31–36 (2004).

5. Bournel, A., Dollfus, P., Bruno, P. & Hesto, P. Gate-induced spin precession in an $In_{0.53}Ga_{0.47}As$ two dimensional electron gas. *Eur. Phys. J. Appl. Phys.* **4,** 1–4 (1998).

6. Mal'shukov, A. G. & Chao, K. A. Waveguide diffusion modes and slowdown of D'yakonov-Perel' spin relaxation in narrow two-dimensional semiconductor channels. *Phys. Rev. B* **61,** R2413–R2416 (2000).

7. Kiselev, A. A. & Kim, K. W. Progressive suppression of spin relaxation in two-dimensional channels of finite width. *Phys. Rev. B* **61,** 13115–13120 (2000).

8. Crooker, S., Baumberg, J., Flack, F., Samarth, N. & Awschalom, D. Terahertz Spin Precession and Coherent Transfer of Angular Momenta in Magnetic Quantum Wells. *Phys. Rev. Lett.* **77,** 2814–2817 (1996).

9. Ramsay, A. J. A review of the coherent optical control of the exciton and spin states of semiconductor quantum dots. *Semicond. Sci. Technol.* **25,** 103001 (2010).

10. Tang, J. & Wang, K. L. Electrical Spin Injection and Transport in Semiconductor Nanowires: Challenges, Progress and Perspectives. *Nanoscale* 4325–4337 (2015). doi:10.1039/C4NR07611G

11. Walther Gerlach, O. S. Der experimentelle Nachweis der Richtungsquantelung im Magnetfeld. *Zeitschrift für Phys.* **9,** 349–352 (1922).

12. Wu, M. W., Jiang, J. H. & Weng, M. Q. Spin dynamics in semiconductors. *Phys. Rep.* **493,** 61–236 (2010).

13. Schulthess, T. C., Temmerman, W. M., Szotek, Z., Butler, W. H. & Malcolm Stocks, G. Electronic structure and exchange coupling of Mn impurities in III–V semiconductors. *Nat. Mater.* **4,** 838–844 (2005).

14. Akai, H. Ferromagnetism and Its Stability in the Diluted Magnetic Semiconductor (In, Mn)As. *Phys. Rev. Lett.* **81,** 3002–3005 (1998).

15. A. Akimov,V. L. Korenev, V. F. Sapega, L. Langer1, S. V. Zaitsev, Yu. A. Danilov, D. R. Yakovlev, M. B. Orientation of electron spins in hybrid ferromagnet–semiconductor nanostructures. *Phys. status solidi* **1672,** 1663–1672 (2014).

16. Kawakami, R. K. *et al.* Ferromagnetic imprinting of nuclear spins in semiconductors. *Science* **294,** 131–4 (2001).

17. F. Meier and B. P. Zachachrenya. *Optical orientation*. (North Holland, 1984).

18. Overhauser, A. W. Polarization of nuclei in metals. *Phys. Rev.* **4,** (1953).

19. Bloch, F. Generalized Theory of Relaxation. *Phys. Rev.* **105,** 1206–1222 (1957).

20. Hahn, E. Spin Echoes. *Phys. Rev.* **80,** 580–594 (1950).

21. Kikkawa, J. M. & Awschalom, D. D. Resonant Spin Amplification in n -Type GaAs. *Phys. Rev. Lett.* **80,** 4313–4316 (1998).

22. D'yakonov, M. I. & Perel', V. I. Spin Orientation of Electrons Associated with the Interband Absorption of Light in Semiconductors. *Sov. physics, JETP* **33,** 1053 (1971).

23. D'yakonov, M. I. & Perel', V. I. No Title. *Sov. physics, Solid State* **13,** 3023 (1972).

24. Dymnikov, V. D., D, M. I. & Perel, N. I. Electrons and Polarization of Hot Luminescence on Semiconductors. *Sov. physics, JETP* **44,** 1252–1256 (1976).

25. Pfalz, S. *et al.* Optical orientation of electron spins in GaAs quantum wells. *Phys. Rev. B* **71,** 165305 (2005).

26. J. M. Kikkawa, I. P. Smorchkova, N. Samarth, D. D. A. & Awschalom, D. D. Lateral drag of spin coherence in gallium arsenide. **397,** 139–141 (1999).

27. Kato, Y. K., Myers, R. C., Gossard, A. C. & Awschalom, D. D. Current-Induced Spin Polarization in Strained Semiconductors. *Phys. Rev. Lett.* **93,** 176601 (2004).

28. Beschoten, B. *et al.* Spin coherence and dephasing in GaN. *Phys. Rev. B* **63,** 3–6 (2001).

29. Kato, Y. K., Myers, R. C., Gossard, A. C. & Awschalom, D. D. Observation of the spin Hall effect in semiconductors. *Science* **306,** 1910–3 (2004).

30. Sih, V. *et al.* Generating spin currents in semiconductors with the spin hall effect. *Phys. Rev. Lett.* **97,** 1–4 (2006).

31. Kato, Y. Electrical Manipulation of Electron Spin Coherence in Nonmagnetic Semiconductors. (UNIVERSITY OF CALIFORNIA Santa Barbara, 2005).

32. J. M. Kikkawa, I. P. Smorchkova, N. Samarth, D. D. A. Room-Temperature Spin Memory in Two-Dimensional Electron Gases. *Science (80-.).* **277,** 1284–1287 (1997).

33. Sih, V. a., Johnston-Halperin, E. & Awschalom, D. D. Optical and electronic manipulation of spin coherence in semiconductors. *Proc. IEEE* **91,** 752–760 (2003).

34. Klövekorn, P. & Munch, J. Variable optical delay line with diffraction-limited autoalignment. *Appl. Opt.* **37,** 1903–1904 (1998).

35. D. D. Awschalom, D. Loss, and N. S. (eds. . *Semicondoctor Spintronics and Quantum Computation*. (Springer Verlag, 2002).

36. Fiederling, R. *et al.* Injection and detection of a spin-polarized current in a light-emitting diode. **402,** 787–790 (1999).

37. Ohno, Y. *et al.* Electrical spin injection in a ferromagnetic semiconductor heterostructure. **402,** 790–792 (1999).

38. Lou, X. *et al.* Electrical detection of spin transport in lateral ferromagnet–semiconductor devices. *Nat. Phys.* **3,** 197–202 (2007).

39. Tserkovnyak, Y., Brataas, A. & Bauer, G. E. W. Enhanced Gilbert Damping in Thin Ferromagnetic Films. *Phys. Rev. Lett.* **88,** 117601 (2002).

40. Tserkovnyak, Y., Brataas, A. & Bauer, G. E. W. Spin pumping and magnetization dynamics in metallic multilayers. *Phys. Rev. B* **66,** 224403 (2002).

41. Heinrich, B. *et al.* Dynamic Exchange Coupling in Magnetic Bilayers. *Phys. Rev. Lett.* **90,** 187601 (2003).

42. Saitoh, E., Ueda, M., Miyajima, H. & Tatara, G. Conversion of spin current into charge current at room temperature: Inverse spin-Hall effect. *Appl. Phys. Lett.* **88,** 182509 (2006).

43. Uchida, K. *et al.* Observation of the spin Seebeck effect. *Nature* **455,** 778–81 (2008).

44. Uchida, K. *et al.* Spin Seebeck insulator. *Nat. Mater.* **9,** 894–7 (2010).

45. Jaworski, C. M. *et al.* Observation of the spin-Seebeck effect in a ferromagnetic semiconductor. *Nat. Mater.* **9,** 898–903 (2010).

46. Xiao, J., Bauer, G. E. W., Uchida, K., Saitoh, E. & Maekawa, S. Theory of magnon-driven spin Seebeck effect. *Phys. Rev. B* **81,** 214418 (2010).

47. Slachter, A., Bakker, F. L., Adam, J.-P. & van Wees, B. J. Thermally driven spin injection from a ferromagnet into a non-magnetic metal. *Nat. Phys.* **6,** 879–882 (2010).

48. Putikka, W. O. & Joynt, R. Theory of optical orientation in n -type semiconductors. *Phys. Rev. B* **70,** 113201 (2004).

49. Bronold, F. X., Martin, I., Saxena, A. & Smith, D. L. Magnetic-field dependence of electron spin relaxation in n -type semiconductors. *Phys. Rev. B* **66,** 233206 (2002).

50. Harmon, N. J., Peterson, T., Geppert, C., Crowell, P., and Flatté, M. E. *(submitted)*

51. Li, Y. *et al.* Inversion of Ferromagnetic Proximity Polarization by MgO Interlayers. *Phys. Rev. Lett.* **100,** 237205 (2008).

52. Lu, Y. *et al.* Band structure of the epitaxial Fe/MgO/GaAs(001) tunnel junction studied by x-ray and ultraviolet photoelectron spectroscopies. *Appl. Phys. Lett.* **89,** 152106 (2006).

53. Uchiyama, H. *et al.* Fabrication of sub-transistor via holes for small and efficient power amplifiers using highly selective GaAs/InGaP wet etching. *J. Vac. Sci. Technol. B Microelectron. Nanom. Struct.* **24,** 664 (2006).

54. Kawakami, R. K. *et al.* Ferromagnetic imprinting of nuclear spins in semiconductors. *Science* **294,** 131–4 (2001).

55. Epstein, R. *et al.* Spontaneous spin coherence in n-GaAs produced by ferromagnetic proximity polarization. *Phys. Rev. B* **65,** 121202 (2002).

56. Ciuti, C., McGuire, J. P. & Sham, L. J. Spin Polarization of Semiconductor Carriers by Reflection off a Ferromagnet. *Phys. Rev. Lett.* **89,** 156601 (2002).

57. C. Weisbuch, C. Hermann, G. F. *Proceedings of the Twelfth International Conference on the Physics of Semiconductors*. (Vieweg+Teubner Verlag, 1974).

58. Paget, D., Lampel, G., Sapoval, B. & Safarov, V. I. Low field electron-nuclear spin coupling in gallium arsenide under optical pumping conditions. *Phys. Rev. B* **15,** 5780–5796 (1977).

59. Perel', M. I. D'yakonov, V. I. No Title. *Sov. J. Exp. Theor. Phys.* **38,** 177 (1984).

60. J. M. Kikkawa, D. D. A. All-Optical Magnetic Resonance in Semiconductors. *Science (80-.).* **287,** 473–476 (2000).

61. Salis, G. *et al.* Optical Manipulation of Nuclear Spin by a Two-Dimensional Electron Gas. *Phys. Rev. Lett.* **86,** 2677–2680 (2001).

62. Salis, G., Awschalom, D. D., Ohno, Y. & Ohno, H. Origin of enhanced dynamic nuclear polarization and all-optical nuclear magnetic resonance in GaAs quantum wells. *Phys. Rev. B* **64,** 195304 (2001).

63. L. L. Buishvili, N. P. Giorgadze, A. I. U. No Title. *Fiz. Tverd. Tela* **16,** 3043 (1974).

64. Harmon, N. J. & Flatté, M. E. Distinguishing Spin Relaxation Mechanisms in Organic Semiconductors. *Phys. Rev. Lett.* **110,** 176602 (2013).

65. Harmon, N. J. & . E. Spin relaxation in materials lacking coherent charge transport. *Phys. Rev. B* **90,** 115203 (2014).

66. Simon M. Sze, M.-K. L. *Semiconductor Devices: Physics and Technology*. (Wiley, 2012).

67. Hohage, P. E., Bacher, G., Reuter, D. & Wieck, A. D. Coherent spin oscillations in bulk GaAs at room temperature. *Appl. Phys. Lett.* **89,** 231101 (2006).

68. Zhu, H. J. *et al.* Room-Temperature Spin Injection from Fe into GaAs. *Phys. Rev. Lett.* **87,** 016601 (2001).

69. Hanbicki, A. T., Jonker, B. T., Itskos, G., Kioseoglou, G. & Petrou, A. Efficient electrical spin injection from a magnetic metal/tunnel barrier contact into a semiconductor. *Appl. Phys. Lett.* **80,** 1240 (2002).

70. Strand, J., Schultz, B. D., Isakovic, A. F., Palmstrøm, C. J. & Crowell, P. A. Dynamic Nuclear Polarization by Electrical Spin Injection in Ferromagnet-Semiconductor Heterostructures. *Phys. Rev. Lett.* **91,** 036602 (2003).

71. Jiang, X. *et al.* Highly Spin-Polarized Room-Temperature Tunnel Injector for Semiconductor Spintronics using MgO(100). *Phys. Rev. Lett.* **94,** 056601 (2005).

72. Crooker, S. A. *et al.* Imaging spin transport in lateral ferromagnet/semiconductor structures. *Science* **309,** 2191–5 (2005).

73. Hirsch, J. E. Spin Hall Effect. *Phys. Rev. Lett.* **83,** 1834–1837 (1999).

74. Lou, X. *et al.* Electrical Detection of Spin Accumulation at a Ferromagnet-Semiconductor Interface. *Phys. Rev. Lett.* **96,** 176603 (2006).

75. Appelbaum, I., Huang, B. & Monsma, D. J. Electronic measurement and control of spin transport in silicon. *Nature* **447,** 295–8 (2007).

76. Jonker, B. T., Kioseoglou, G., Hanbicki, A. T., Li, C. H. & Thompson, P. E. Electrical spin-injection into silicon from a ferromagnetic metal/tunnel barrier contact. *Nat. Phys.* **3,** 542–546 (2007).

77. Pareek, T. P. & Bruno, P. Spin coherence in a two-dimensional electron gas with Rashba spin-orbit interaction. *Phys. Rev. B* **65,** 241305 (2002).

78. Holleitner, A. W., Sih, V., Myers, R. C., Gossard, A. C. & Awschalom, D. D. Suppression of Spin Relaxation in Submicron InGaAs Wires. *Phys. Rev. Lett.* **97,** 036805 (2006).

79. Thelander, C. *et al.* Nanowire-based one-dimensional electronics. *Mater. Today* **9,** 28–35 (2006).

80. Lauhon, L. J., Gudiksen, M. S., Wang, D. & Lieber, C. M. Epitaxial core-shell and core-multishell nanowire heterostructures. *Nature* **420,** 57–61 (2002).

81. Samuelson, L. *et al.* Semiconductor nanowires for novel one-dimensional devices. *Phys. E Low-dimensional Syst. Nanostructures* **21,** 560–567 (2004).

82. Huang, Y., Duan, X., Cui, Y. & Lieber, C. M. Gallium Nitride Nanowire Nanodevices. *Nano Lett.* **2,** 101–104 (2002).

83. Pettersson, H. *et al.* Infrared photodetectors in heterostructure nanowires. *Nano Lett.* **6,** 229–32 (2006).

84. Noborisaka, J., Motohisa, J., Hara, S. & Fukui, T. Fabrication and characterization of freestanding GaAs⁄AlGaAs core-shell nanowires and AlGaAs nanotubes by using selective-area metalorganic vapor phase epitaxy. *Appl. Phys. Lett.* **87,** 093109 (2005).

85. Dubrovskii, V. G. *et al.* Shape modification of III-V nanowires: The role of nucleation on sidewalls. *Phys. Rev. E* **77,** 031606 (2008).

86. Givargizov, E. Fundamental aspects of VLS growth. *J. Cryst. Growth* **31,** 20–30 (1975).

87. Johansson, J., Svensson, C. P. T., Mårtensson, T., Samuelson, L. & Seifert, W. Mass transport model for semiconductor nanowire growth. *J. Phys. Chem. B* **109,** 13567–71 (2005).

88. Borgström, M., Deppert, K., Samuelson, L. & Seifert, W. Size- and shape-controlled GaAs nano-whiskers grown by MOVPE: a growth study. *J. Cryst. Growth* **260,** 18–22 (2004).

89. Seifert, W. *et al.* Growth of one-dimensional nanostructures in MOVPE. *J. Cryst. Growth* **272,** 211–220 (2004).

90. Joyce, H. J. *et al.* Twin-free uniform epitaxial GaAs nanowires grown by a two-temperature process. *Nano Lett.* **7,** 921–6 (2007).

91. Joyce, H. *et al.* Tailoring GaAs, InAs, and InGaAs nanowires for optoelectronic device applications. *IEEE J. Sel. Top. Quantum Electron.* **17,** 766–778 (2011).

92. Joyce, H. J. *et al.* High Purity GaAs Nanowires Free of Planar Defects: Growth and Characterization. *Adv. Funct. Mater.* **18,** 3794–3800 (2008).

93. Joyce, H. J. *et al.* Unexpected benefits of rapid growth rate for III-V nanowires. *Nano Lett.* **9,** 695–701 (2009).

94. Titova, L. V. *et al.* Temperature dependence of photoluminescence from single core-shell GaAs–AlGaAs nanowires. *Appl. Phys. Lett.* **89,** 173126 (2006).

95. Skromme, B. J. & Stillman, G. E. Excited-state-donor-to-acceptor transitions in the photoluminescence spectrum of GaAs and InP. *Phys. Rev. B* **29,** 1982–1992 (1984).

96. Hiruma, K. *et al.* Growth and optical properties of nanometer-scale GaAs and InAs whiskers. *J. Appl. Phys.* **77,** 447 (1995).

97. Guo, J. *et al.* Realizing Zinc Blende GaAs/AlGaAs Axial and Radial Heterostructure Nanowires by Tuning the Growth Temperature. *J. Mater. Sci. Technol.* **27,** 507–512 (2011).

98. Fortuna, S. A., Wen, J., Chun, I. S. & Li, X. Planar GaAs nanowires on GaAs (100) substrates: self-aligned, nearly twin-defect free, and transfer-printable. *Nano Lett.* **8,** 4421–4427 (2008).

99. Novoselov, K. S. *et al.* Electric field effect in atomically thin carbon films. *Science* **306,** 666–9 (2004).

100. Novoselov, K. S. *et al.* Two-dimensional atomic crystals. *Proc. Natl. Acad. Sci. U. S. A.* **102,** 10451–3 (2005).

101. Geim, A. K. & Novoselov, K. S. The rise of graphene. *Nat. Mater.* **6,** 183–91 (2007).

102. Geim, A. K. Graphene: status and prospects. *Science (80-.).* **324,** 1530–4 (2009).

103. Butler, S. Z. *et al.* Progress, challenges, and opportunities in two-dimensional materials beyond graphene. *ACS Nano* **7,** 2898–2926 (2013).

104. Novoselov, K. S. *et al.* A roadmap for graphene. *Nature* **490,** 192–200 (2012).

105. Abergel, D. S. L., Apalkov, V., Berashevich, J., Ziegler, K. & Chakraborty, T. Properties of Graphene: A Theoretical Perspective. *Adv. Phys.* **59,** 261–482 (2010).

106. Han, W., Kawakami, R. K., Gmitra, M. & Fabian, J. Graphene spintronics. *Nat. Nanotechnol.* **9,** 794–807 (2014).

107. Liu, C. C., Feng, W. & Yao, Y. Quantum spin Hall effect in silicene and two-dimensional germanium. *Phys. Rev. Lett.* **107,** 1–4 (2011).

108. Xu, Y. *et al.* Large-gap quantum spin hall insulators in tin films. *Phys. Rev. Lett.* **111,** 1–5 (2013).

109. Gupta, G. *et al.* Y-shape spin-separator for two-dimensional group-IV nanoribbons based on quantum spin hall effect. *Appl. Phys. Lett.* **104,** (2014).

110. Tse, W. K., Saxena, a., Smith, D. L. & Sinitsyn, N. a. Spin and valley noise in two-dimensional Dirac materials. *Phys. Rev. Lett.* **113,** 1–5 (2014).

111. Rachel, S. & Ezawa, M. Giant magnetoresistance and perfect spin filter in silicene, germanene, and stanene. *Phys. Rev. B - Condens. Matter Mater. Phys.* **89,** 1–6 (2014).

112. Kohl, M., Freeman, M. R., Awschalom, D. D. & Hong, J. M. Femtosecond spectroscopy of carrier-spin relaxation in GaAs- Al x Ga 1 − x As quantum wells. *Phys. Rev. B* **44,** 5923–5926 (1991).

113. Amand, T. *et al.* Exciton formation and hole-spin relaxation in intrinsic quantum wells. *Phys. Rev. B* **50,** 11624–11628 (1994).

114. Yao, W., Xiao, D. & Niu, Q. Valley-dependent optoelectronics from inversion symmetry breaking. *Phys. Rev. B* **77,** 235406 (2008).

115. Cao, T. *et al.* Valley-selective circular dichroism of monolayer molybdenum disulphide. *Nat. Commun.* **3,** 887 (2012).

116. Zeng, H., Dai, J., Yao, W., Xiao, D. & Cui, X. Valley polarization in MoS2 monolayers by optical pumping. *Nat. Nanotechnol.* **7,** 490–3 (2012).

117. Nijamudheen, a., Bhattacharjee, R., Choudhury, S. & Datta, A. Electronic and Chemical Properties of Germanene: The Crucial Role of Buckling. *J. Phys. Chem. C* **119,** 3802–3809 (2015).

118. Wang, J., Deng, S., Liu, Z. & Liu, Z. The rare two-dimensional materials with Dirac cones. *Natl. Sci. Rev.* **2,** 22–39 (2015).

119. Bianco, E. *et al.* Stability and exfoliation of germanane: A germanium graphane analogue. *ACS Nano* **7,** 4414–4421 (2013).

120. Jiang, S., Arguilla, M. Q., Cultrara, N. D. & Goldberger, J. E. Covalently-Controlled Properties by Design in Group IV Graphane Analogues. *Acc. Chem. Res.* **48,** 144–151 (2015).

121. Jiang, S. *et al.* Improving the stability and optical properties of germanane via one-step covalent methyl-termination. *Nat. Commun.* **5,** 3389 (2014).

122. Zheng, J., Chi, F. & Guo, Y. Enhanced spin Seebeck effect in a germanene p-n junction. *J. Appl. Phys.* **116,** 243907 (2014).

123. Delerue, C. Prediction of robust two-dimensional topological insulators based on Ge/Si nanotechnology. *Phys. Rev. B* **90,** 075424 (2014).

124. Seixas, L., Padilha, J. E. & Fazzio, a. Quantum spin Hall effect on germanene nanorod embedded in completely hydrogenated germanene. *Phys. Rev. B* **89,** 1–5 (2014).

125. Pinchuk, I. V. *et al.* Epitaxial co-deposition growth of CaGe2 films by molecular beam epitaxy for large area germanane. *J. Mater. Res.* **29,** 410–416 (2014).

126. Odenthal, P. M. Optical Characterization of Two Dimensional Semiconductors. Ph.D thesis, University of California Riverside, 2015.